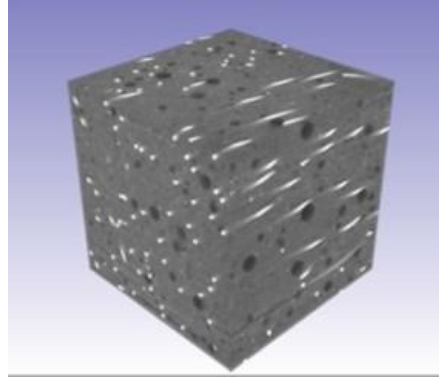


Durability and Smart Condition Assessment of Ultra-High Performance Concrete in Cold Climates



Pizhong Qiao, Ph.D., P.E.
Zhidong Zhou, Graduate Research Assistant
Srinivas Allena, Ph.D., P.E.
Department of Civil and Environmental Engineering
Washington State University
Pullman, WA 99164-2910

Date: 12/31/2016

Prepared by: Pizhong Qiao and Zhidong Zhou

Center for Environmental Sustainable
Transportation in Cold Climates
University of Alaska Fairbanks
Duckering Building, Room 245
P.O. Box 755900
Fairbanks, AK 99775

U.S. Department of Transportation
1200 New Jersey Avenue, SE
Washington, D.C. 20590

INE/AUTC 17.06



REPORT DOCUMENTATION PAGE			Form approved OMB No.	
Public reporting for this collection of information is estimated to average 1 hour per response, including the time for reviewing instructions, searching existing data sources, gathering and maintaining the data needed, and completing and reviewing the collection of information. Send comments regarding this burden estimate or any other aspect of this collection of information, including suggestion for reducing this burden to Washington Headquarters Services, Directorate for Information Operations and Reports, 1215 Jefferson Davis Highway, Suite 1204, Arlington, VA 22202-4302, and to the Office of Management and Budget, Paperwork Reduction Project (0704-1833), Washington, DC 20503				
1. AGENCY USE ONLY (LEAVE BLANK)	2. REPORT DATE 12/31/2016	3. REPORT TYPE AND DATES COVERED Final Report: 11/2015 – 12/2016		
4. TITLE AND SUBTITLE Durability and Smart Condition Assessment of Ultra-High Performance Concrete in Cold Climates			5. FUNDING NUMBERS	
6. AUTHOR(S) Pizhong Qiao, Ph.D., P.E. Zhidong Zhou, Graduate Research Assistant Srinivas Allena, Ph.D., P.E. Dept. of Civil & Environmental Engineering, Washington State University, Pullman, WA				
7. PERFORMING ORGANIZATION NAME(S) AND ADDRESS(ES) Center for Environmentally Sustainable Transportation in Cold Climates University of Alaska Fairbanks Duckering Building, Room 245 P.O. Box 755900 Fairbanks, AK 99775-5900			8. PERFORMING ORGANIZATION REPORT NUMBER	
9. SPONSORING/MONITORING AGENCY NAME(S) AND ADDRESS(ES) U.S. Department of Transportation 1200 New Jersey Avenue, SE Washington, DC 20590			10. SPONSORING/MONITORING AGENCY REPORT NUMBER	
11. SUPPLEMENTARY NOTES				
12a. DISTRIBUTION / AVAILABILITY STATEMENT No restrictions			12b. DISTRIBUTION CODE	
13. ABSTRACT (Maximum 200 words) The goals of this study were to develop ecological ultra-high performance concrete (UHPC) with local materials and supplementary cementitious materials and to evaluate the long-term performance of UHPC in cold climates using effective mechanical test methods, such as “smart aggregate” technology and microstructure imaging analysis. The optimal UHPC mixture approximately exhibited compressive strength of 15 ksi, elastic modulus of 5,000 ksi, direct tensile strength of 1.27 ksi, and shrinkage of 630 µε at 28 days, which are characteristics comparable to those of commercial products and other studies. The tensile strength and modulus of elasticity in tension, dynamic modulus, and wave modulus show slight increases from the original values after 300 freeze-thaw (F-T) cycles, indicating that UHPC has excellent frost resistance in cold climates. Although porosity deterioration was observed in the F-T cyclic conditioning process, no internal damage (cracks or fractures) was found during imaging analysis up to 300 cycles. Since structures for which UHPC would be used are expected to have a longer service life, more F-T cycles are recommended to condition UHPC and investigate its mechanical performance over time. Moreover, continuum damage mechanic-based models have the potential to evaluate damage accumulation in UHPC and its failure mechanism under frost attack and to predict long-term material deterioration and service life.				
14. KEYWORDS : Ultra-high performance concrete (UHPC); mechanical properties; durability; smart aggregate; freezing and thawing cyclic conditioning; service life.			15. NUMBER OF PAGES 80	
			16. PRICE CODE N/A	
17. SECURITY CLASSIFICATION OF REPORT Unclassified	18. SECURITY CLASSIFICATION OF THIS PAGE Unclassified	19. SECURITY CLASSIFICATION OF ABSTRACT Unclassified	20. LIMITATION OF ABSTRACT N/A	

Durability and Smart Condition Assessment of Ultra-High Performance Concrete in Cold Climates

Final Report

Pizhong Qiao, Ph.D., P.E.
Zhidong Zhou, Graduate Research Assistant
Srinivas Allena, Ph.D., P.E.
Department of Civil and Environmental Engineering
Washington State University
Pullman, WA 99164-2910

Prepared by:

Pizhong Qiao and Zhidong Zhou

Prepared for

Center for Environmentally Sustainable
Transportation in Cold Climates
University of Alaska Fairbanks
Duckering Building, Room 245
P.O. Box 755900
Fairbanks, AK 99775

and

U.S. Department of Transportation
1200 New Jersey Avenue, SE
Washington, D.C. 20590

December 31, 2016 (Revised on March 26, 2017)

INE/AUTC 17.06

DISCLAIMER

This document is disseminated under the sponsorship of the U.S. Department of Transportation in the interest of information exchange. The U.S. Government assumes no liability for the use of the information contained in this document. The U.S. Government does not endorse products or manufacturers. Trademarks or manufacturers' names appear in this report only because they are considered essential to the objective of the document.

Opinions and conclusions expressed or implied in the report are those of the author(s). They are not necessarily those of the funding agencies.

METRIC (SI*) CONVERSION FACTORS

APPROXIMATE CONVERSIONS TO SI UNITS

APPROXIMATE CONVERSIONS FROM SI UNITS

Symbol	When You Know	Multiply By	To Find	Symbol
<u>LENGTH</u>				
in	inches	25.4	mm	mm
ft	feet	0.3048	m	m
yd	yards	0.914	m	m
mi	Miles (statute)	1.61	km	km
<u>AREA</u>				
in ²	square inches	645.2	millimeters squared	cm ²
ft ²	square feet	0.0929	meters squared	m ²
yd ²	square yards	0.836	meters squared	m ²
mi ²	square miles	2.59	kilometers squared	km ²
ac	acres	0.4046	hectares	ha
<u>MASS (weight)</u>				
oz	Ounces (avdp)	28.35	grams	g
lb	Pounds (avdp)	0.454	kilograms	kg
T	Short tons (2000 lb)	0.907	megagrams	mg
<u>VOLUME</u>				
fl oz	fluid ounces (US)	29.57	milliliters	mL
gal	Gallons (liq)	3.785	liters	liters
ft ³	cubic feet	0.0283	meters cubed	m ³
yd ³	cubic yards	0.765	meters cubed	m ³
Note: Volumes greater than 1000 L shall be shown in m ³				
<u>TEMPERATURE (exact)</u>				
°F	Fahrenheit temperature	5/9 (°F-32)	Celsius temperature	°C
<u>ILLUMINATION</u>				
fc	Foot-candles	10.76	lux	lx
fl	foot-lamberts	3.426	candela/m ²	cd/cm ²
<u>FORCE and PRESSURE or STRESS</u>				
lbf	pound-force	4.45	newtons	N
psi	pound-force per square inch	6.89	kilopascals	kPa

Symbol	When You Know	Multiply By	To Find	Symbol																								
<u>LENGTH</u>																												
mm	millimeters	0.039	inches	in																								
m	meters	3.28	feet	ft																								
m	meters	1.09	yards	yd																								
km	kilometers	0.621	Miles (statute)	mi																								
<u>AREA</u>																												
mm ²	millimeters squared	0.0016	square inches	in ² m ²																								
meters squared		10.764	square feet	ft ² km ²																								
kilometers squared		0.39	square miles	mi ² ha																								
hectares (10,000 m ²)		2.471	acres	ac																								
<u>MASS (weight)</u>																												
g	grams	0.0353	Ounces (avdp)	oz																								
kg	kilograms	2.205	Pounds (avdp)	lb mg																								
megagrams (1000 kg)		1.103	short tons	T																								
<u>VOLUME</u>																												
mL	milliliters	0.034	fluid ounces (US)	fl oz																								
liters	liters	0.264	Gallons (liq)	gal																								
m ³	meters cubed	35.315	cubic feet	ft ³																								
m ³	meters cubed	1.308	cubic yards	yd ³																								
<u>TEMPERATURE (exact)</u>																												
°C	Celsius temperature	9/5 °C+32	Fahrenheit temperature	°F																								
<u>ILLUMINATION</u>																												
lx	lux	0.0929	foot-candles	fc																								
cd/cm ²	candela/m ²	0.2919	foot-lamberts	fl																								
<u>FORCE and PRESSURE or STRESS</u>																												
N	newtons	0.225	pound-force	lbf																								
kPa	kilopascals	0.145	pound-force per square inch	psi																								
<table style="width: 100%; border: none;"> <tr> <td style="width: 15%;"></td> <td style="width: 10%;"></td> <td style="width: 10%; text-align: center;">32</td> <td style="width: 10%; text-align: center;">98.6</td> <td style="width: 10%;"></td> <td style="width: 10%; text-align: center;">212°F</td> </tr> <tr> <td style="text-align: center;">-40°F</td> <td style="text-align: center;">0</td> <td style="text-align: center;">40</td> <td style="text-align: center;">80</td> <td style="text-align: center;">120</td> <td style="text-align: center;">160</td> </tr> <tr> <td style="text-align: center;">-40°C</td> <td style="text-align: center;">-20</td> <td style="text-align: center;">20</td> <td style="text-align: center;">40</td> <td style="text-align: center;">60</td> <td style="text-align: center;">80</td> </tr> <tr> <td></td> <td></td> <td style="text-align: center;">0</td> <td style="text-align: center;">37</td> <td></td> <td style="text-align: center;">100°C</td> </tr> </table>							32	98.6		212°F	-40°F	0	40	80	120	160	-40°C	-20	20	40	60	80			0	37		100°C
		32	98.6		212°F																							
-40°F	0	40	80	120	160																							
-40°C	-20	20	40	60	80																							
		0	37		100°C																							

These factors conform to the requirement of FHWA Order 5190.1A *SI is the symbol for the International System of Measurements

ACKNOWLEDGMENTS

The authors acknowledge the financial support provided by the Center for Environmentally Sustainable Transportation in Cold Climates (CESTiCC) and the Washington State Department of Transportation (WSDOT). The materials provided by the BASF Corporation and the Nano-CT imaging analysis performed by Professor Lizhi Sun's group at the University of California Irvine (UCI) are gratefully acknowledged. The authors thank Professor John Stanton of the University of Washington, Dr. Bijan Khaleghi of WSDOT, and Lu Sachao of WSDOT for their technical input and support. The authors also appreciate the support and encouragement by Professor and Director Juanyu (Jenny) Liu of CESTiCC and the thorough editing and proofreading of the report by Grace F. Pedersen of the University of Alaska Fairbanks.

TABLE OF CONTENTS

LIST OF FIGURES	iii
LIST OF TABLES	v
EXECUTIVE SUMMARY.....	1
CHAPTER 1. Introduction.....	4
1.1 Problem Statement.....	4
1.2 Research Objectives.....	5
CHAPTER 2. Literature Review	6
2.1 Ultra-High Performance Concrete.....	6
2.2 Properties of UHPC	8
2.2.1 Compressive strength.....	8
2.2.2 Modulus of elasticity.....	10
2.2.3 Tensile strength	11
2.2.4 Shrinkage and creep.....	16
2.3 Durability of UHPC.....	18
2.4 Smart Piezoelectric Sensors/Actuators	19
CHAPTER 3. Materials and Experimental Program	22
3.1 Introduction.....	22
3.2 Development of UHPC.....	22
3.2.1 Raw materials.....	24
3.2.2 Mix designs.....	24
3.2.3 Mixing, casting and curing	26
3.3 Evaluation of the Properties of Fresh and Hardened UHPC	27
3.3.1 Flowability test.....	27
3.3.2 Compressive strength and modulus of elasticity	28
3.3.3 Tensile strength	28
3.3.4 Shrinkage	29
3.4 Durability Tests of UHPC.....	32
3.4.1 Rapid freeze and thaw test.....	32
3.4.2 Dynamic modulus test.....	33
3.4.3 Smart aggregates.....	34
3.4.4 X-ray CT imaging analysis	36
CHAPTER 4. Test Results and Analysis	38

4.1 Results of Fresh and Hardened UHPC	38
4.1.1 Flow tests	38
4.1.2 Compressive strength and modulus of elasticity	38
4.1.3 Tensile strength	41
4.1.4 Shrinkage	45
4.2 Test Results of Durability Study	47
4.2.1 Dynamic modulus and wave modulus	47
4.2.2 Results from direct tension test.....	50
4.2.3 X-ray CT imaging analysis	52
CHAPTER 5. Conclusions and Recommendations	57
5.1 Summary	57
5.2 Findings	57
5.3 Recommendations.....	59
References.....	61

LIST OF FIGURES

Figure 2.1 Sketch of direct tension test (DTT) specimen (Graybeal and Baby 2013).....	14
Figure 2.2 Test setup and instrumentation (Kusumawardaningsih et al. 2015b).....	15
Figure 2.3 Direct tension test (DTT) (Nguyen et al. 2014)	16
Figure 3.1 Flow test of UHPC	27
Figure 3.2 Illustration of the test setup, specimen shape and measurement system.....	29
Figure 3.3 Shrinkage tests of UHPC.....	30
Figure 3.4 Restrained shrinkage test of UHPC.....	32
Figure 3.5 Freeze-thaw conditioning machine.....	33
Figure 3.6 Dynamic modulus test setup at WSU.....	34
Figure 3.7 Fabrication process of smart aggregate	34
Figure 3.8 UPHC specimen with embedded smart aggregates.....	35
Figure 3.9 Wave modulus test setup and typical input and outputs signal	35
Figure 3.10 Xradia 410 Versa X-ray microscope at UCI	37
Figure 4.1 Compressive strengths at different ages and by different size specimens.....	39
Figure 4.2 Modulus of elasticity at different ages and by different size specimens	40
Figure 4.3 Measured and predicted modulus of elasticity	41
Figure 4.4 Comparison of tensile strength.....	42
Figure 4.5 Stress-strain response of UHPC in direct tension with different ages of curing	44
Figure 4.6 Comparisons of modulus of elasticity from the compression and direct tension tests	45
Figure 4.7 Comparison of autogenous shrinkage	46
Figure 4.8 Comparison of free shrinkage	46
Figure 4.9 Restrained shrinkage from ring tests	47
Figure 4.10 Comparison of values of modulus of elasticity by different test methods	48
Figure 4.11 Comparison of dynamic and wave modulus values and their relative modulus ...	49
Figure 4.12 Comparison of surface scaling of UHPC at different F-T cycles.....	50
Figure 4.13 Tensile strength and modulus of elasticity from direct tension test at different F-T cycles	51
Figure 4.14 Stress-strain response of conditioning UHPC in direct tension	52
Figure 4.15 2D and 3D reconstructed slices of UHPC (concrete matrix, gray; steel fibers, white spots; air voids, dark spots).....	53

Figure 4.16 Segmented pores in UHPC at different F-T cycles	54
Figure 4.17 Segmented steel fibers in UHPC at different F-T cycles	54
Figure 4.18 Pore distribution in UHPC at different cycles	55
Figure 4.19 Pore size above 1 mm in UHPC at different cycles	56

LIST OF TABLES

Table 3.1 UHPC mixture proportions	25
Table 4.1 Pore and fiber information in UPHC	54

EXECUTIVE SUMMARY

Ultra-high performance concrete (UHPC) is an advanced cementitious material of enhanced strength and durability compared with conventional concrete, qualities which are of great significance in a wide variety of structural applications. However, the cost of using commercial products in UHPC is high, so developing UHPC mixtures that contain locally available materials and supplementary cementitious materials saves on costs. To use UHPC in Alaska and other northern states, it is necessary to know its approximate service life and long-term durability, and its frost resistance in regions subject to freezing and thawing cycles. The goals of this study were to develop cost-effective UHPC by using local materials and supplementary cementitious materials and to assess the long-term performance of UHPC, particularly in cold regions, by using “smart aggregate” technology in combination with X-ray CT imaging analysis.

Twelve trial UHPC mixtures produced with locally available cement, sand, and admixtures as well as domestic steel fibers were initially evaluated for their workability and compressive strength. One optimal mixture (C3) was selected for further evaluation of its mechanical properties and long-term durability. Expensive materials, such as quartz powder and imported fibers, commonly used in commercial products and other studies, were not used in this study.

The experimental evaluation of UHPC mixture C3 was divided into two categories: (1) its mechanical properties, including compressive and tensile strength, modulus of elasticity, ductility, shrinkage, and tensile strength-related properties, and (2) its durability when subjected to freeze-thaw (F-T) cycles and characterized/assessed using the smart aggregates technique and X-ray CT imaging analysis.

The following findings were determined:

1. The optimal UHPC mixture approximately exhibits compressive strength of 15 ksi, elastic modulus of 5,000 ksi, direct tensile strength of 1.27 ksi, and shrinkage of 630 $\mu\epsilon$ at 28 days. These measurements are comparable to those of commercial products and reported in other studies, and they outweigh the measurements of conventional concrete.

2. The tensile strength and modulus of elasticity in tension, dynamic modulus, and wave modulus show a slight increase from the virgin values after 300 F-T cycles, indicating that UHPC has excellent frost resistance in cold climates.

3. No internal damage (cracks or fractures) was detected through X-ray imaging analysis up to 300 cycles; however, porosity deterioration was observed during the F-T conditioning process, indicating that internal damage would more likely occur if F-T conditioning continued.

The following observations and recommendations will improve the understanding of UHPC and its long-term performance in cold climates:

1. Ultra-high performance concrete structures are expected to have a longer service life than conventional concrete. More F-T conditioning cycles (300 cycles are recommended for the evaluation of normal concrete) or more severe conditioning protocols should be applied to UHPC.

2. Once the degradation of material properties is experimentally evaluated, damage mechanics-based models have the potential to evaluate damage accumulation and failure mechanisms of UHPC under frost attack and to predict long-term material deterioration and service life.

3. It has been established that UHPC exhibits superior resistance to rapid F-T cycles. However, because salty deicers are commonly used in cold regions to melt snow and ice for improved traffic safety, the resistance of UHPC under combined frost and chemical attack should be investigated. The corrosion of steel fibers and corrosion's effects on UHPC performance cannot be neglected.

4. The innovative and effective condition assessment technique using embedded smart aggregates is capable of in situ monitoring of strength growth, assessing long-term durability, and detecting potential damage to UHPC materials and structures.

CHAPTER 1. INTRODUCTION

1.1 Problem Statement

Ultra-high performance concrete (UHPC) is an advanced cementitious material of improved strength and durability compared with conventional concrete. Development and characterization of cost-effective and environmentally friendly UHPC are of significance so that UHPC can be used in a wide variety of structural applications. With the commercially available pre-packaged UHPC product Ductal®, the cost of implementing this material in design is still rather high. To reduce costs, promote wide implementation, and improve the sustainability of UHPC, research is needed to develop UHPC mixtures that contain local materials and supplementary cementitious materials. This objective can be achieved by developing UHPC mixtures that use locally available materials and by replacing the cement and silica fume with more economical materials, such as fly ash and slag at different replacement levels. Selection of these materials is viewed as an improvement in sustainability and will help reduce the cost of UHPC.

In addition to developing UHPC with local materials and supplementary cementitious materials (Qiao et al. 2017), there is a need to investigate the probable life span, early age shrinkage, and long-term durability characteristics of UHPC—alkali silica reaction (ASR) and freeze-thaw (F-T) resistance—particularly in cold regions. Investigations of the long-term performance of UHPC used in new bridge construction (such as bridge deck connection joints) are few. Though studies (Graybeal 2006) indicate that the performance of UHPC shows promise and superior results in comparison with conventional concrete, its long-term performance, particularly in cold climates where concrete is subjected to F-T cycles, is not well studied. There

is a pressing need to develop cost-effective UHPC with local materials and supplementary cementitious materials and to assess UHPC's long-term performance using new smart sensor technology, particularly for applications in cold regions.

Alaska and northern states are faced with unique challenges in maintaining a safe, reliable transportation system. Some of the special challenges include long distances between communities, adverse cold climate conditions, and high transportation costs. These challenges suggest an immediate need to improve the planning, design, construction, maintenance, and operations of cold region transportation infrastructure. The longevity and reliability of concrete transportation infrastructure are strategically critical in improving transportation maintenance and operations in cold regions. In this study, cost-effective UHPC, resilient in cold climates, was developed and characterized; its durability in cold climates was evaluated using accelerated conditioning, smart sensor technology, and nano X-ray computer tomography (CT).

1.2 Research Objectives

Combined with a related work at Washington State Department of Transportation (WSDOT) (Qiao et al. 2017), this study had two objectives: to develop an ecological UHPC with local materials and supplementary cementitious materials and to evaluate the long-term performance of UHPC in cold climates using “smart aggregate” technology. To accomplish these objectives, the research activities were organized into four major tasks:

- Development of UHPC using local materials and supplementary cementitious materials.
- Evaluation of the properties of fresh and hardened UHPC.
- Assessment of the durability of UHPC using embedded smart aggregate technology.
- Development of guidelines and recommendations for developing UHPC in cold regions.

CHAPTER 2. LITERATURE REVIEW

This chapter focuses on past studies conducted on the development of UHPC and the evaluation of its properties. The constituents of UHPC, its strength and durability properties, with emphasis on various specimen sizes and innovative testing methods, and the importance of UHPC in terms of its potential for application in bridge construction have been discussed in detail.

2.1 Ultra-High Performance Concrete

Ultra-high performance concrete, also known as reactive powder concrete (RPC), has a minimum specified compressive strength of 150 MPa (21,750 psi) and a flexural strength greater than 10 MPa (1,450 psi) at 28 days. However, at such high strengths, the coarse aggregate causes the weakest link in concrete (Dili and Santhanam 2004). Development of shear and tensile stresses at the paste-aggregate interface causes cracks in the paste of traditional concrete when compressive force is applied. According to Richard and Cheyrezy (1994), the size of an equatorial crack is directly proportional to the diameter of the aggregate particle. Moreover, the use of coarse aggregate may affect fiber dispersion, fiber embedment, and crack bridging. Thus, the elimination of coarse aggregate greatly improves the homogeneity of concrete and, subsequently, its mechanical strength. This practice has been employed in what is today known as RPC or UHPC. Ultra-high performance concrete is usually produced with cement, fine quartz sand, silica fume, steel fibers, and high range water-reducing admixture (HRWRA). Very low ratios of water to cementitious materials, ranging between 0.15 and 0.25, are used to produce this kind of concrete.

Ultra-high performance concrete differs from conventional concrete not only in strength but also in durability. This concrete is more durable because the lower ratio of water to cementitious materials results in exceptionally low porosity (Roux et al. 1996). Ultra-high performance concrete with a compressive strength of 160 MPa (23,200 psi), developed by Ji et al. (2007), was used in the sidewalk systems of the Qinghai-Tibet Railway bridge, built on frozen earth. Ji et al. (2007) reported that UHPC exhibited superior frost durability and impermeability. By using UHPC, the size or number of structural members can be reduced, which is economically beneficial to the construction industry (Brooks and Wainright 1983). However, evaluation of the long-term behavior of UHPC is needed before the concrete is widely used in transportation infrastructure. In ultra-high strength silica fume concrete, appreciable basic creep was observed, whereas drying creep was negligible and drying shrinkage was small (Brooks and Hynes 1996). Allena and Newtonson (2011) developed UHPC using local materials with compressive and flexural strengths of 170.3 MPa (24,700 psi) and 18.3 MPa (2,650 psi), and they quantified early age (within the first 24 hours) and long-term shrinkage.

Roux et al. (1996) demonstrated that the mechanical properties of RPC are obtained by lowering the ratio of water to cementitious materials and by including HRWRA and silica fume. The lower water-to-cementitious material ratio reduces the porosity of the cement paste and improves durability. The following steps were taken in developing UHPC to achieve its high strength and long-term performance properties:

1. Removal of coarse aggregate to enhance the concrete's homogeneity.
2. Use of silica fume for pozzolanic reaction.
3. Optimization of the granular mixture to enhance compacted density.
4. Application of presetting pressure for better compaction.

5. Post-setting heat treatment to enhance the mechanical properties of the microstructure.
6. Addition of steel fibers to achieve ductility.

In addition, optimization of granular mixtures can be achieved by calculating packing density (the ratio of volume of solids to the total unit volume) and using packing models such as the solid suspension model (SSM) for granular mixtures (Lerrard and Sedran 1994).

2.2 Properties of UHPC

Standard and non-standard test methods conducted on traditional concrete have been extended to characterize UHPC and determine its material properties, including compressive and tensile strength, modulus of elasticity, shrinkage, and creep.

2.2.1 Compressive strength

Ultra-high performance concrete usually has a compressive strength above 150 MPa (21,750 psi) at 28 days, with superior mix designs and treatments. The compressive strength of UHPC is strongly related to testing, curing conditions, geometry of specimen, and mix constituents.

Curing regimes have an effect on the compressive strength of UHPC, since environmental temperature and humidity significantly affect the cement hydration process. Graybeal (2007) conducted experiments on 3-by-6-inch cylinders by applying steam curing and laboratory curing after demolding. Steam-cured specimens exhibited a compressive strength of 193 MPa (28 ksi) at 28 days, while untreated specimens produced a compressive strength of 126 MPa (18.3 ksi) at 28 days.

Fiber content also significantly influences the compressive strength of UHPC. Kusumawardaningsinh et al. (2015a) compared the compressive strength of UHPC cubes with fiber contents of 0%, 1%, and 2% by volume. The corresponding compressive strengths were

166.4 MPa, 176.27 MPa, and 178.03 MPa, respectively. Kusumawardaningsinh et al. concluded that steel fibers enhanced the compressive strength of the UHPC. This phenomenon was observed in failure modes as well; i.e., the plain UHPC specimens failed with sudden, explosive brittle failure, while the fiber-reinforced UHPC specimens exhibited ductile failure.

There are two types of compression test specimens for concrete: cylinders and cubes. In the United States, the popular specimen geometry is in form of a cylinder. Even though this method is efficient and economical when used for testing conventional concrete, a few practical problems are encountered when using cylinder specimens for testing UHPC's compressive strength. To get accurate results from this test, the ends of the cylinder must have flat, planar surfaces to take the force exerted by the testing machine. ASTM C617 (2015) and ASTM C1231 (2015) provide guidelines for preparing the cylinder ends with capping compounds, but the strength of these compounds is limited, so this technique is not useful with UHPC. An alternative technique is to grind the ends of the cylinders, but this technique is time-consuming and expensive. Using a cube is an alternative to using a cylinder and eliminates some of these issues. ASTM C109 (2016), which is based on 2-inch cubes for testing hydraulic cement mortars, can be used with UHPC, which is essentially a mortar as it does not contain coarse aggregate. Additionally, the aspect ratio of a specimen subjected to uniaxial loading affects the compression behavior, leading to cubes having greater compressive strength than cylinders (Neville 1996). Graybeal (2015), who conducted extensive tests on compressive strength with various geometries of cubes and cylinders to characterize the effects of size on the compressive strength of UHPC, concluded that smaller specimens showed greater compressive strength than larger specimens, and cubes had higher compressive strength than cylinders.

Since the compressive strength of UHPC can exceed the compressive strength of concrete by a factor of 7 (Graybeal 2015), using the standard ASTM C39 (2016) to measure the compressive strength of UHPC can cause a few concerns. In addition to problems related to the end preparation of cylinders (mentioned previously), the loading rate is an issue. Using the specified loading rate in ASTM C39 (35 psi/s) for testing UHPC specimens would result in a longer test duration. Graybeal (2015) studied the effects of using higher loading rates ranging up to 220 psi/s for testing UHPC compression test specimens. Several variables were included in the study: age of concrete at testing, curing conditions, geometry of specimen, and mix constituents. The typical time duration of testing a conventional concrete specimen at 35 psi/s was 3 minutes. When testing UHPC specimens at a rate of 150 psi/s, the time duration was also approximately 3 minutes. Therefore, this rate was selected as the appropriate reference point to compare results. It was concluded that increasing the load rate had a minimal effect on the observed strength.

2.2.2 Modulus of elasticity

In the study by Graybeal (2007), steam-treated UHPC had a modulus of elasticity of 52.7 GPa (7,650 ksi) with a 1.5 standard deviation at 28 days. At the same test time, the untreated specimens displayed an elastic modulus of 42.7 GPa (6,200 ksi). It was concluded that the modulus of elasticity of UHPC was predictable within a compressive strength range of 25–193 MPa (3.6–28 ksi). In a newer study by Graybeal (2015), the modulus of elasticity was in the range of 50–55 GPa (7,300–8,000 ksi) in accordance with ASTM C469. Steam-cured as well as laboratory-cured cylinder specimens with 3- and 4-inch diameters were tested with axial strain measurement devices to record the change in length. The same issue mentioned previously related to compressive strength was also considered in this study. The loading rate was changed

to increase up to 200 psi/s. However, the increase in the loading rate from 35–150 psi/s did not have a significant effect on the observed elastic modulus of UHPC.

2.2.3 Tensile strength

2.2.3.1 Flexural strength (modulus of rupture)

Colleparidi et al. (1997) investigated the flexural strength of RPC specimens. Flexural strengths were determined at 3, 7, and 28 days, using a third-point loading method on 150 mm × 150 mm × 600 mm (6 inch × 6 inch × 24 inch) beams and a central point loading method on 40 mm × 40 mm × 160 mm (1.6 inch × 1.6 inch × 6.5 inch) specimens. Specimens were cured at three different temperatures: 20°C, 90°C, and 160°C. At 28 days, the flexural strengths in the third-point loading tests were 16.1–21.6 MPa, while the central point loading test yielded results of 35.5–60.1 MPa, indicating that the smaller beams exhibited greater flexural strength. The flexural strength was reduced when all fine sand was replaced by coarse aggregate. The authors explained that the reasons for lower flexural strength were material homogeneity and bond strength.

The modulus of rupture values from Russel and Graybeal (2013) were obtained using the standard ASTM C1018 (1997, withdrawn 2006). The strengths for the first cracking varied from 9.0–10.3 MPa (1.3–1.5 ksi), depending on the method of steam curing, while the values were lower for untreated specimens, about 9.0 MPa (1.3 ksi). ASTM C78 (2016) was used by Allena and Newtonson (2011) to measure the modulus of rupture. The specimen size was 75 mm × 100 mm × 400 mm (3 inch × 4 inch × 16 inch), and the specimens were rotated 90° from the orientation in which they were cast to apply the loading. At the age of 7 days, the modulus of rupture values were 10–18.3 MPa (1.45–2.65 ksi).

2.2.3.2 Splitting tensile strength

Karmout (2009) measured the splitting tensile strength according to ASTM C496 (2011), which is an indirect method of measuring the tensile strength of concrete. This method is usually used to evaluate the shear resistance provided by the constituents in the concrete matrix. The compressive load applied along the length of the cylinder induces tensile and shear stress on the aggregate elements in the specimen, generating bond failure between aggregate particles and the cement paste. Karmout (2009) used the cylinder specimens of 150 mm in diameter and 300 mm in height and obtained the tensile strengths of 6.3, 7.1, and 8.1 MPa at 7, 14, and 28 days, respectively.

Graybeal and Hartmann (2003) also used the testing procedure based on ASTM C496 with a few modifications; the load rate was increased from 100–200 psi/min (0.690–1.379 MPa/min) to 500 psi/min (3.447 MPa/min) to reduce the testing time duration. Preliminary testing had been done to ensure that this change would not significantly affect the results. Also, lateral expansion of the specimen was measured during the test by a spring-loaded apparatus which held two displacement transducers at each end of the specimen. The specimen size was 101.6 mm (4 inch) in diameter and 203.2 mm (8 inch) in height. The tensile cracking strength, which was obtained at the point where the specimen lateral stiffness changes initially, was the greatest for steam-cured (194°F, 95% RH [relative humidity] for 48 hours after demolding) specimens; 11.7 MPa (1.7 ksi) at 28 days. Tempered steam-cured (140°F, 95% RH for 48 hours after demolding) specimens showed a slightly lower strength of 11.0 MPa (1.6 ksi), while the ambient air-cured specimens indicated a strength of 9.0 MPa (1.3 ksi) at 28 days. The peak strength values were also presented, but these results were not taken as accurate representations of the actual tensile strength of UHPC, since the loading configuration of the test causes a biaxial

state of stress, which produced the significantly increased fiber pullout strength. The steam-cured specimens exhibited the highest tensile strength of 24.2 MPa (3.51 ksi) at 28 days, while the ambient air-treated specimens had a strength of 19.0 MPa (2.75 ksi) at 28 days.

2.2.3.3 Direct tension strength

The tensile strength of concrete can also be measured directly. Graybeal and Hartmann (2003) measured tensile strength in this direct method, which is similar to the compression test, except that the ends of the cylinder are adhesively bonded to the testing machine. This method is based on the RILEM uniaxial tension test for steel fiber-reinforced concrete (RILEM, 2001) and USBR 4914 (USBR, 1992) test methods. The specimen was 4 inches in diameter and 8 inches in height. The cracking strengths for the various curing conditions were as follows: Steam-cured (194°F, 95% RH for 48 hours after demolding) specimens had a tensile strength of 11.0 MPa (1.6 ksi), and delayed steam-cured specimens had a strength of 11.2 MPa (1.62 ksi). However, the air-cured specimens had a significantly lower strength of 5.65 MPa (0.82 ksi).

Graybeal and Baby (2013) designed another direction tension test (DTT) specimen to capture the tensile behavior of UHPC accurately, with a 50.8 mm (2 inch) square cross section and 431.8 mm (17 inch) or 304.8 mm (12 inch) in length. Tapered aluminum plates were glued with high strength epoxy to the ends of the UHPFRC prism to limit the crack location inside the gauge length, and the strain was measured with a parallel ring extensometer (Figure 2.1). The specimens were subjected to both steam curing and laboratory environment curing. The first cracking strengths for steam-cured and air-cured specimens with 431.8 mm (17 inch) long specimens were 9.09 MPa (1.32 ksi) and 6.67 MPa (0.97 ksi), respectively, and the 304.8 mm (12 inch) long specimens had lower strengths comparatively. The use of longer specimens was hence recommended by the authors.

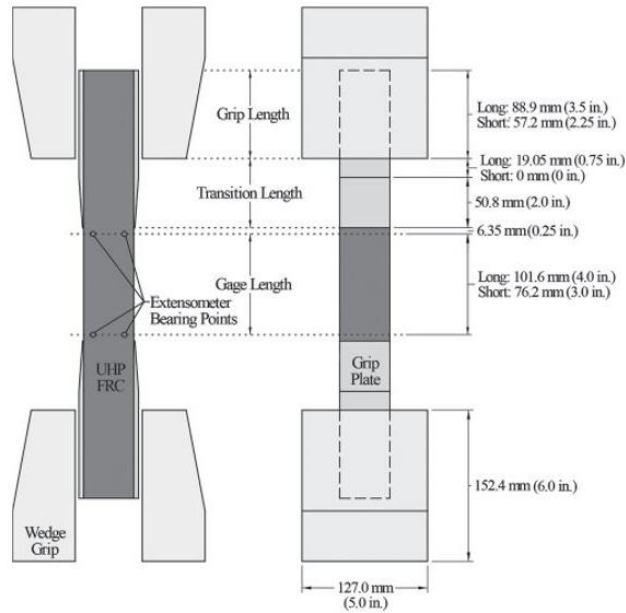


Figure 2.1 Sketch of direct tension test (DTT) specimen (Graybeal and Baby 2013)

Another approach taken by Kusumawardaningsih et al. (2015b) was to cast a series of prisms with a cross section of 40 mm × 40 mm, but with a 5 mm × 5 mm notch in the middle, as shown in Figure 2.2. It was observed that the maximum tensile strength of plain UHPC was approximately 4 MPa with sudden brittle failure, while UHPC with 2% fiber reinforcement was about 6.6 MPa, the maximum tensile strength, and exhibited excellent ductile behavior.

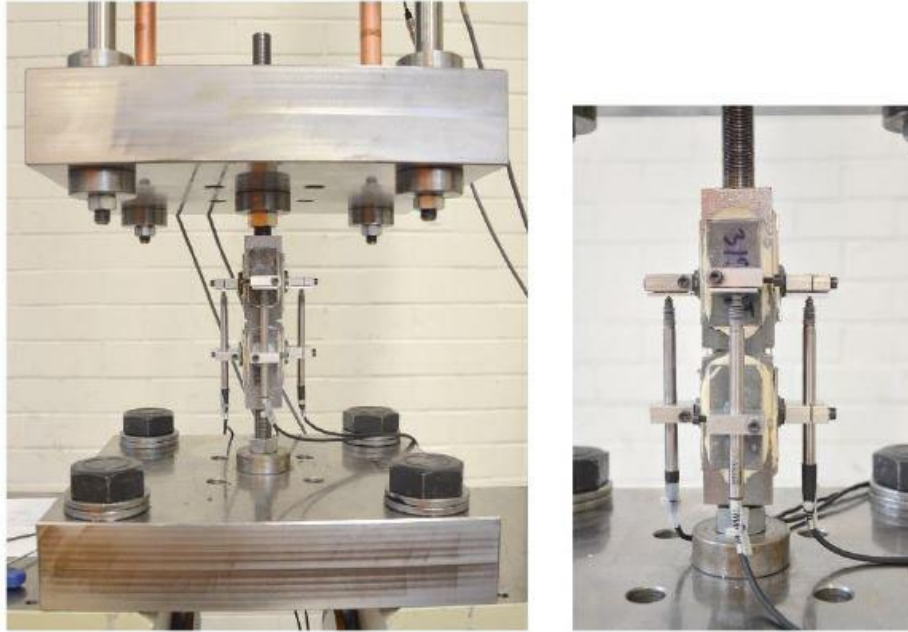


Figure 2.2 Test setup and instrumentation (Kusumawardaningsih et al. 2015b)

Nguyen et al. (2014) investigated the effects of size and geometry on the direct tensile stress of UHPC using dogbone-shaped specimens (Figure 2.3). Gauge length, section area, volume, and thickness were considered, and strength, strain capacity, and energy absorption capacity were obtained eventually. The increasing of gauge length, section area, and volume of specimens resulted in a little reduction of tensile strength, but a significant decrease in strain capacity and energy absorption capacity and a clear increase in the crack spacing of specimens. However, it was observed that the tensile strength increased slightly, and both the strain capacity and energy absorption capacity distinctly increased when the thickness of the specimen was increased. Tran et al. (2015) concluded that the specimen size clearly influences the tensile strength of UHPC at high strain rates.

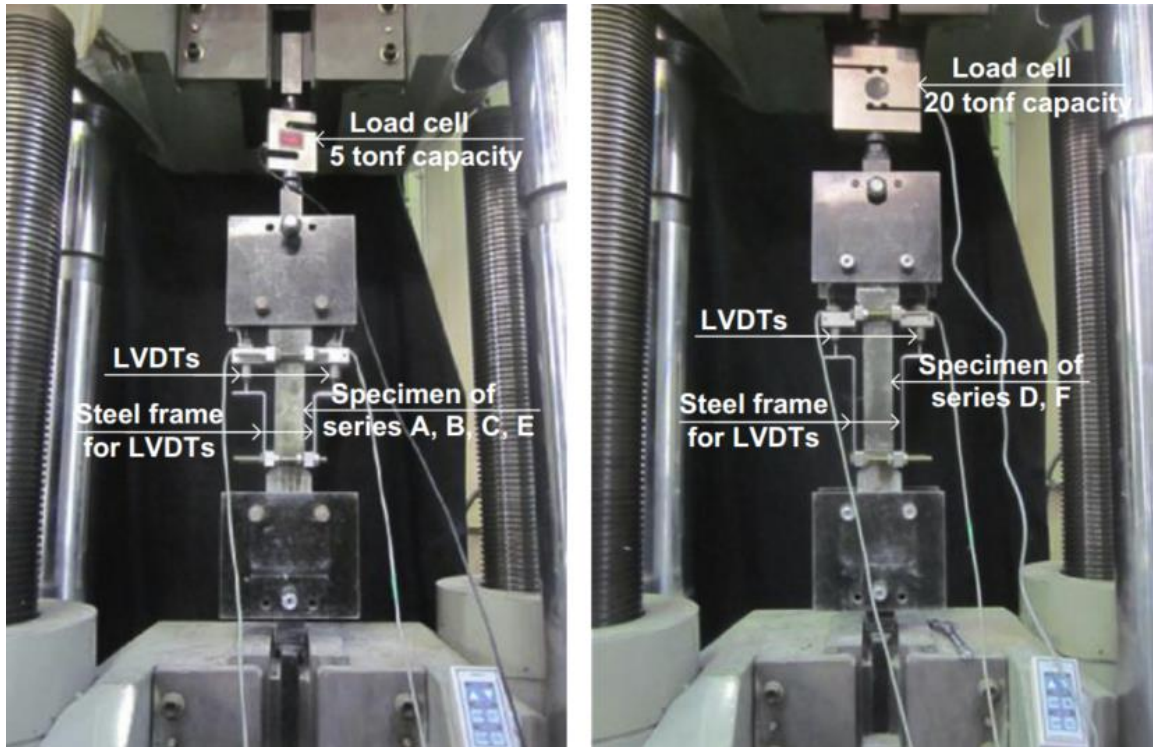


Figure 2.3 Direct tension test (DTT) (Nguyen et al. 2014)

The strain rate dependent properties of UHPC under direct tension were investigated by Pyo et al. (2015). The dogbone-shaped specimens with different fiber content and fiber type were tested under different strain rates, which varied from 0.0001 1/s to 0.1 1/s. Pyo et al. observed that tensile strength and fracture energy increased with the increase of strain rate and fiber volume.

2.2.4 Shrinkage and creep

The quantity of water in a concrete mix greatly affects its shrinkage characteristics. Shrinkage is a result of changes in the volume of the concrete due to loss of water from the mix. Concrete with high w/cm tends to shrink more than concrete with low w/cm because the excess water flows to the concrete surface. When this occurs, the excess water evaporates from the surface of the concrete, leaving cracks on the concrete surface. The types of shrinkage associated with concrete are plastic, autogenous, drying, and carbonation shrinkage (Shetty 2005).

Shrinkage-swelling behavior was observed by Collepardi et al. (1997) in mixtures with coarse aggregate partially or wholly replacing sand or cementitious material, after a curing time of 7 days. The specimens were exposed to 65% RH air for 30 days and submerged in water. There was no significant difference in shrinkage or swelling between the mixes, whether coarse aggregate was included. Shrinkage was also lower in steam-cured and autoclaved specimens when compared with the air-cured specimens. After a month of exposure to 65% air, the shrinkage was about 600 $\mu\epsilon$.

Graybeal and Hartmann (2003) conducted a limited shrinkage study to observe the early age shrinkage behavior of UHPC. The specimen was 25 mm \times 25 mm \times 275 mm (1 inch \times 1 inch \times 11 inch) in size, and 6 bars each were tested for each curing condition based on ASTM C157 (2014). The air-cured specimens exhibited the most shrinkage at 620 $\mu\epsilon$ in 28 days, while the steam-cured specimens exhibited the lowest shrinkage, about 500 $\mu\epsilon$ in 4.1 days.

Since measuring autogenous shrinkage is a somewhat complex task, no standard method is established. Eppers and Muller (2008) measured linear autogenous shrinkage under quasi-isothermal conditions (20°C) using prisms with a dimension of 25 mm \times 25 mm \times 285 mm. The specimens were sealed with stainless steel foil, tape, and beeswax; therefore, temperature changes and heat of hydration were neglected. Mechanically coupled sensors were employed to measure shrinkage, which at the age of 28 days was approximately 600–900 $\mu\epsilon$. The strains were higher with lower water/cement ratios and with high silica fume contents. Steel fibers reduced the strain by 10–15%.

Collepardi et al. (1997), who presented results from creep tests performed on RPC as well, reported that the creep strain of the UHPC specimens under stress of 53 MPa (7,685 psi) with a stress-strength ratio of 1/3 at the time of loading was greater than the creep strain of

normal strength concrete, with compressive strength ranging from 30 to 40 MPa (4,350 to 5,800 psi). However, the ultimate specific creep including elastic strain was $35 \times 10^{-6} \text{ MPa}^{-1}$ ($0.241 \times 10^{-6} \text{ psi}^{-1}$), regardless of the stress-strength ratio and aggregate-to-cement ratio of the original or modified RPC. They also reported that the specific creep of autoclaved specimens was lower than that of specimens cured at room temperature, and the creep of specimens cured at room temperature was the same as that of normal strength concrete.

2.3 Durability of UHPC

Durability issues, such as water absorption, chloride penetration, freeze-thaw (F-T) durability, and delayed ettringite formation, are critical to UHPC as well. Excessive water absorption by concrete leads to scaling of material when the concrete is exposed to freezing and thawing. This scaling can eventually lead to corrosion of the reinforcement due to penetration of chloride ions, particularly in tidal areas (Roux et al. 1996). Dili and Santhanam (2004) compared the water absorption rate of UHPC and HPC, and observed a similar trend of decreasing water absorption with age; however, the percentage of water absorption by UHPC was low compared with that of HPC. The presence of chloride ions near reinforcing steel in concrete structures is a major cause of corrosion. If the chloride ion concentration exceeds the threshold value, the passivating layer on the reinforcing steel is destroyed; the chloride ions act as a catalyst for corrosion. Hence, the study of chloride ion concentration and the impermeable nature of concrete is of importance. The chloride ion penetration was greater when the HPC specimens were heat cured (Dili and Santhanam 2004), and the chloride penetration was due to the incorporation of fibers in the specimens, leading to the increased conductance of concrete. However, it was reported that the resistance to chloride ion penetration of RPC was superior to that of HPC. As

expected, UHPC has excellent resistance to freezing and thawing as well (Shaheen and Shrive 2006).

Delayed ettringite formation (DEF) may occur when a cement of high sulfate content or a gypsum-contaminated aggregate has been used in concrete production (Mehta and Monteiro 2006). Ettringite decomposes to form monosulfate hydrate at elevated temperatures. Sulfate ions are released, and these sulfate ions are absorbed by C-S-H gel. Ettringite is later re-formed when sulfate ions are desorbed. This re-formation of ettringite causes expansion that leads to deterioration. Delayed ettringite formation can only occur in heat-cured specimens on subsequent cooling (Diamond 1996; Mindess et al. 2003; Taylor et al. 2001). According to Collepardi (2003), the factors essential for DEF-related damage include the following: microcracks caused by factors such as alkali-silica reaction (ASR), exposure to water or saturated air, and late sulfate release. Several studies have been conducted on DEF, primarily for conventional concrete (Kelham 1996; Ronne and Hammer 1999; Tosun 2006).

2.4 Smart Piezoelectric Sensors/Actuators

With advances in sensor and wireless communication technologies, it is now increasingly feasible to monitor and assess the condition of concrete structures in situ. The smart piezoelectric sensors and actuators are capable of monitoring the property changes and conditions (including damage), especially the long-term performance, of structural concrete. Piezoelectric materials can generate a charge in response to mechanical stimulus (sensor action), or alternatively provide a mechanical strain when an electric field is applied across them (actuator action). The piezo-wafer can be used as an actuator to generate excitation for both dynamic vibration and wave transmission. These materials exhibit excellent mechanical strength and have low acoustic impedance, flat response over a wide frequency range, and broad dynamic response. The

piezoelectric materials can be tailored to a specific size or application and are easily incorporated into other structures; they are also increasingly affordable (Zou et al. 2000). Repeatability of the experiment is crucial in damage detection, which greatly depends on the repeatability of the excitation forces. In vibration testing, the piezoelectric actuator bonded to or embedded in the structure provides the best repeatability in actuation compared with others, such as impact hammer and electromagnetic shaker (Luo and Hanagud 1999). Piezoelectric material, lead zirconate titanate (called PZT), is a kind of smart material that has been used for detecting defects in concrete structures in recent years. The PZT patches are small, lightweight, and inexpensive, and they can be used as both actuators and sensors by leveraging their piezoelectric effect. The two types of PZT-based active damage detection methods include (1) the impedance-based method and (2) the elastic wave-based method (Wu and Chang 2006 a,b; Song et al. 2006, 2008; Yan et al. 2009; Qiao et al. 2010). The impedance-based method uses high-frequency structural excitations, typically higher than 20 kHz (Park et al. 2006), and employs bonded or embedded PZT patches to capture changes in the mechanical impedance of a structure. Based on changes in the impedances obtained by the PZT patches, the damages in the structure can be located and identified (Tseng and Wang 2004; Wen et al. 2007; Yang et al. 2008; Shin et al. 2008; Talakokula et al. 2013; Cahill et al. 2014; Jung et al. 2014).

Recently, Qiao et al. (2010) developed a damage detection technique using embedded smart aggregates that could determine the severity of crack damage in unreinforced concrete beams. The signal energy of the first shear wave package can be used to indicate the presence of and approximately quantify the extent of the crack damage. The health monitoring technique using embedded smart aggregates also exhibits its capability of in situ assessment of the change of modulus of elasticity (MOE) due to F-T conditioning cycles in concrete beams. The

degradation (e.g., MOE reduction) trend concluded from the wave propagation test was consistent with that from the dynamic modulus test based on the frequency measurement (Qiao and Chen 2013). Further research is needed to apply the embedded smart piezoelectric modules (so-called smart aggregates) and associated wave propagation-based health-monitoring technique for assessing the degradation process in concrete.

CHAPTER 3. MATERIALS AND EXPERIMENTAL PROGRAM

In this chapter, combined with a related study by WSDOT (Qiao et al. 2017), the experimental testing programs to evaluate fresh and hardened properties of UHPC are presented. These tests include flowability, compressive and tensile strength, modulus of elasticity, shrinkage, and durability assessment.

3.1 Introduction

The scope of this study included development of the UHPC mixture design with locally available materials and supplementary cementitious materials, evaluation of fresh and hardened properties of UHPC, and long-term performance assessment of UHPC using embedded smart aggregate technology in simulated cold climates and repeated cycles of freezing and thawing. Smart aggregates, which are capable of assessing the material properties during curing as well as in hardened concrete, and of monitoring long-term performance, were embedded in UHPC. The UHPC was developed with consideration of locally available materials and supplementary cementitious materials. The resiliency and sustainability of UHPC leading to green transportation construction in cold climates are demonstrated, and the potential and usefulness of smart aggregate technology is evaluated by assessing the performance and monitoring the durability of UHPC under coupled freezing and thawing cycles, simulating severe weather conditions in cold climates.

3.2 Development of UHPC

Ultra-high performance concrete is a material technological breakthrough with the potential to transform the product design and service life of precast concrete. The greatest

implication of UHPC is in sustainable transportation infrastructure development. The application of UHPC may lead to smaller member sizes, which would reduce the volume of concrete required to produce a given structural element. More durable structures are possible when using UHPC. However, as sustainable development is currently a crucial global issue and various industries are striving to save energy and lower environmental impacts, the high material cost, high energy consumption, and embedded carbon dioxide for existing and commercial UHPC are factors that restrict its wider application. The materials used in UHPC mixtures are often shipped long distances, internationally in many cases, increasing the cost of the materials. Additionally, strict requirements on the chemistry of the cement and silica fume increase the cost of commercially available prepackaged UHPC products. Therefore, sustainability in terms of reduced cost and environmental impact must be achieved to encourage greater use of UHPC in highway infrastructure and for other structural applications.

This study focused on pursuing the following measures: use of locally available materials, industrial by-products (such as fly ash and blast furnace slag as a partial replacement for cement and silica fume), and development of a simplified energy-efficient curing method to produce low-cost, eco-friendly UHPC. The steel fibers considered in this research were obtained locally (domestically), unlike commercial UHPC with imported steel fibers. Each selection of local materials is seen as an improvement in developing cost-effective and sustainable UHPC. Steam curing and heat treatment are commonly employed curing methods for UHPC. However, heat treatment of UHPC specimens at extremely high temperatures is impractical in a precast plant or in the field. Therefore, a simplified curing methodology needs to be developed without compromising mechanical strength.

3.2.1 Raw materials

Portland cement Type I-II with a specific gravity of 3.15 was used to prepare the UHPC samples. Commercially available silica fume (Rheomac SF 100), provided by BASF Construction Chemicals, LLC, was used as a partial replacement of cement to improve the mechanical properties and durability of UHPC.

Local natural sand was provided by Atlas Sand & Rock, located in Pullman, Washington. The sand passed through the ASTM No. 30 (0.6 mm) sieve and over the No. 200 (0.075 mm) sieve, and was washed to remove the clay/silt particles and then oven-dried at 110°C (230°F) to achieve zero moisture content. The specific gravity and water absorption of the fine sand were determined according to ASTM C128 (2015), and are 2.60 and 2.6%, respectively.

Domestically available steel fibers (NYCON-SF Type I), provided by Nycon Corporation, were used to enhance the durability and toughness of UHPC. The steel fibers were added at a content of 2% by volume, which is commonly recommended for UHPC reinforcement.

Glenium 3030 NS, a commercially available polycarboxylate-based high range water-reducing admixture (HRWRA) produced by BASF Construction Chemicals, LLC was used in the UHPC mixes to achieve the desired workability.

3.2.2 Mix designs

As shown in Table 3.1, twelve trial mixtures with varying ratios of water–cementitious materials (w/cm), and different amounts of silica fume, cement, and HRWRA were considered. Primarily based on flowability and compressive strength, one mixture proportion of UHPC (C3) was chosen for further study of its durability performance.

Table 3.1 UHPC mixture proportions

Mixture Type	Unit	A1	A2	A3	A4	A5	B1	B2	B3	B4	C1	C2	C3
Type I/II Portland Cement	lb/yd ³	1500	1475	1500	1500	1500	1450	1390	1278	1500	1620	1560	1500
Silica Fume	lb/yd ³	375	150	375	375	375	195	190	320	375	260	260	260
Fine Sand	lb/yd ³	1396	1823	1297	1355	1374	1864	1906	1860	1436	1463	1521	1574
Steel Fibers	lb/yd ³	267	197	267	240	267	197	197	197	237	236	236	236
HRWRA	gal/yd ³	7	7	7	7	8	8.7	9.0	9.5	9.0	9.5	10.5	11.5
Water	lb/yd ³	375	330	413	394	375	288	290	280	347	347	335	325
w/cm		0.20	0.20	0.22	0.21	0.20	0.18	0.18	0.18	0.18	0.18	0.18	0.18
Spread Testing	in.	6.50	7.00	7.75	9.00	7.75	5.00	6.00	5.50	5.75	7.25	8.00	9.50

3.2.3 Mixing, casting and curing

Mixing of constituents to produce specimens of UHPC was conducted at the concrete laboratory at Washington State University (WSU) using a portable mixer with a volume of 10 gallons. The entire mixing time was relatively longer than that for conventional concrete due to the elimination of coarse aggregate and the use of low w/cm ratios. Mixing time also depended on the power of the mixer. The mixing time of the portable laboratory mixer ranged from 16–20 minutes and consisted of four stages: (1) mix the dry constituents 2–3 minutes, (2) add 75% of the water and mix 4–5 minutes, (3) add the HRWRA and the remaining 25% of water and mix 2 minutes, and (4) add the steel fibers and continue mixing 8–10 minutes till thoroughly combined.

As soon as the mixing was completed, the fresh UHPC was poured into oiled wooden/steel molds to cast specimens in accordance with ASTM C192 (2016). Specimens were externally vibrated for approximately 5–10 seconds using a vibrating table. The amount of vibration time depended on the consistency of the mix. After approximately 24 hours, specimens were demolded and the curing period began.

Due to the very low water content of UHPC, it is extremely critical to prevent loss of internal water due to evaporation and keep specimens in a high moisture environment immediately after casting. The curing of UHPC specimens consists of two phases: initial curing after casting and standard curing prior to testing. All specimens in the molds were cured in a vibration-free fog room with a temperature of $23.0 \pm 2.0^{\circ}\text{C}$ ($73.5 \pm 3.5^{\circ}\text{F}$) from the time of casting. All specimens were demolded after 24 ± 4 hours from casting and then soaked in lime-saturated water in storage tanks until testing age.

3.3 Evaluation of the Properties of Fresh and Hardened UHPC

After developing UHPC mixtures, the fresh and hardened properties of UHPC were evaluated. The basic material tests (e.g., strength, modulus, shrinkage, etc.) were conducted according to the standard ASTM test methods. In particular, early-age and long-term shrinkage characteristics and the effect of steel fibers on shrinkage along with other mechanical properties were studied. This portion of the study advances research conducted by others to develop UHPC because previous work focused almost exclusively on strength development and mechanical properties. Achieving greater strength alone is not sufficient, but the process involved should be energy efficient and environmentally sustainable.

3.3.1 Flowability test

The flow table test for hydraulic cement mortar is widely employed on fresh UHPC to evaluate its rheology. Once mixing was completed, the flow test was conducted following the procedures of ASTM C1437 (2015) (Figure 3.1), that is, immediately dropping the flow table 25 times in 15 seconds after lifting the flow mold away, and then measuring the average diameter of flow of the UHPC mix.



Figure 3.1 Flow test of UHPC

3.3.2 Compressive strength and modulus of elasticity

To investigate size effects on the compressive strength of UHPC, three types of specimens were tested: 2-inch cubes, 4-inch cubes, 3-inch × 6-inch cylinders, and 4-inch × 8-inch cylinders. The compressive strength tests were conducted following the procedures of ASTM C109 and ASTM C39. The modulus of elasticity test was conducted following the procedures of ASTM C469.

3.3.3 Tensile strength

3.3.3.1 Flexural strength (modulus of rupture)

The flexural strength test was performed in accordance with ASTM C78. A constant loading rate was applied under a specific tensile stress rate within the range of 125 to 175 psi/min.

3.3.3.2 Splitting tensile strength

The splitting tensile strength test was conducted following the procedures of ASTM C496. The required range of splitting tensile stress is 100 to 200 psi/min; thus, the corresponding loading rate should be in the range of 11,300 to 22,600 lbf/min for 6-inch × 12-inch cylinders.

3.3.3.3 Direct tensile strength

The UHPC dogbone specimens for direct tension were designed and fabricated with a net cross section of 2 inches × 2 inches and a gauge length of 6 inches (Figure 3.2). Two bolts with caps were embedded inside the ends of the sample for connecting the specimen to the testing machine grasps. An extensometer with a 2-inch gauge length was used to measure the tensile strain. To assure tensile strength under quasi-static state, a very low loading rate (i.e., 0.0001 in/s) was chosen.

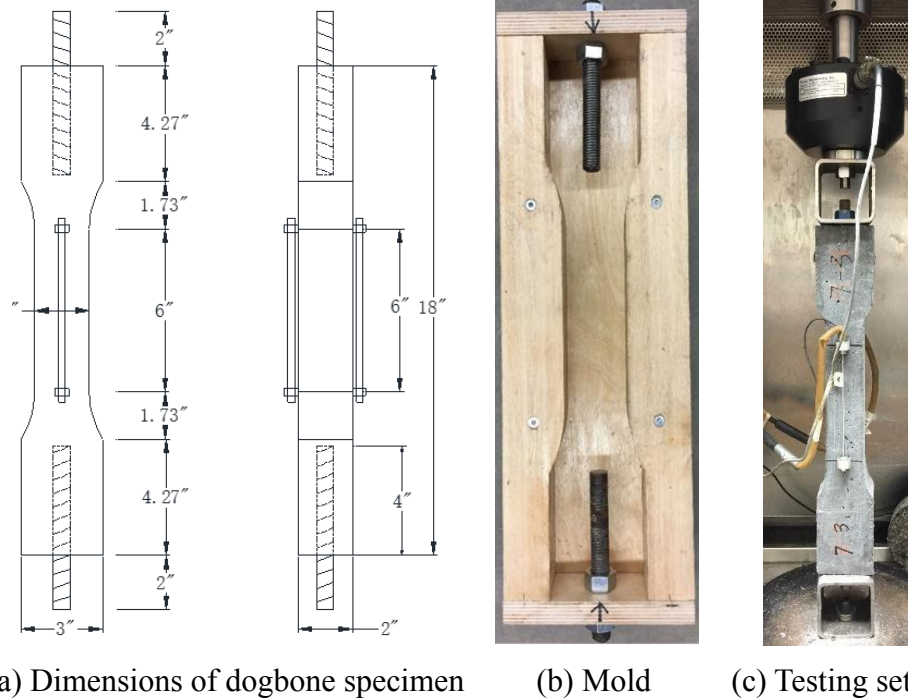


Figure 3.2 Illustration of the test setup, specimen shape and measurement system

3.3.4 Shrinkage

Autogenous shrinkage is due to hydration of the binder in UHPC; drying shrinkage is due to moisture loss when UHPC is exposed to a dry environment. The shrinkage test of UHPC was conducted in accordance with ASTM C157 (2014) “Standard Test Method for Length Change of Hardened Hydraulic-Cement Mortar and Concrete.” Two geometries of prism specimens were fabricated to investigate the size effect on shrinkage: (a) 1 inch \times 1 inch \times 11.25 inch, and (b) 4 inch \times 4 inch \times 11.25 inch. The length change of the 4-inch \times 4-inch \times 11.25-inch prism was measured after 24 hours from casting by a linear variable differential transformer (LVDT) glued at two ends and automatically collected by the data acquisition system. The shrinkage of the 1-inch \times 1-inch \times 11.25-inch prism was measured by digital gauges at two ends (Figure 3.3). The surface of the UHPC specimens used for the autogenous shrinkage test was sealed with a thin layer of epoxy, followed by plastic wrap to prevent moisture loss. The prisms without sealer

were used to monitor the free shrinkage, which consists of autogenous shrinkage and dry shrinkage. The UHPC specimens used for the drying shrinkage test were cured at a curing room with a temperature of $73 \pm 3^\circ\text{F}$ ($23 \pm 2^\circ\text{C}$) and relative humidity of $50 \pm 4\%$.



(a) Autogenous and free shrinkage tests of the 4-inch \times 4-inch \times 11.25-inch prism



(b) Autogenous and free shrinkage tests of the 1-inch \times 1-inch \times 11.25-inch prism

Figure 3.3 Shrinkage tests of UHPC

The free shrinkage tests mainly provide the basic moisture-related shrinkage characteristics of UHPC without any restraint. In most cases, however, concrete is under different boundary conditions, and shrinkage-induced tension may lead to cracking behaviors. Both the ASTM and the AASHTO provide test methods for restrained shrinkage measurement, and suggest the ring test for determining the relative cracking tendency among different concrete mixtures under certain drying conditions. The test methods of the ASTM and the AASHTO are based on the same theory and procedures; however, the dimensions of the concrete ring and the allowable nominal sizes of coarse aggregate show some differences.

The AASHTO T334-08 (2012), “Standard Method of Test for Estimating the Cracking Tendency of Concrete,” was adopted in this study for restrained shrinkage measurement. The

inside steel ring was cut from a steel tube for industry (allowable in the AASHTO standard); it had an outer diameter of 12.75 inches, a wall thickness of $1/2 \pm 1/64$ inch, and a height of 6 inches (Figure 3.4a). The outside ring was made of a plastic board with a thickness of 0.25 inch and an inner diameter of 18 inches, and was supported around by plywood. The steel strains were measured by four strain gauges equidistantly mounted on the inner surface of the inside steel ring and automatically recorded by SmartStrain software at an interval of 1 s (Figure 3.4d). The UHPC ring was casted intermediately after mixing and covered with wet burlap, followed by a plastic sheet to prevent moisture loss from the specimens for the first day. After this initial curing, the outer plastic board was demolded, and the top surface was coated with a thin layer of paraffin wax to prevent moisture loss (Figures 3.4b and 3.4c). The ring specimen of UHPC was allowed to present water evaporation through the outside surface only. Similar to free shrinkage, all UHPC specimens used in the restrained shrinkage test were cured at a curing room with a temperature of $73 \pm 3^\circ\text{F}$ ($23 \pm 2^\circ\text{C}$) and relative humidity of $50 \pm 4\%$.



(a) Restrained steel ring setup



(b) After casting with UHPC



(c) UHPC ring after demolding

(d) Data acquisition system

Figure 3.4 Restrained shrinkage test of UHPC

3.4 Durability Tests of UHPC

Apart from standard test protocol (e.g., ASTM C215 [2014]), other methods were adopted to evaluate the frost resistance of UHPC, including the use of smart aggregates, X-ray CT imaging, and direct tension testing. The UHPC specimens were subjected to accelerated freeze-thaw (F-T) conditioning, and their long-term properties were monitored and measured with smart aggregates. In parallel, the dynamic modulus and nano-CT images of the UHPC samples at different defined F-T cycles were accordingly obtained. Direct tension tests were also conducted on dogbone specimens with certain F-T conditioning cycles to characterize the durability of the specimens in terms of tensile strength and strain hardening.

3.4.1 Rapid freeze and thaw test

The manufactured UHPC prism samples were conditioned using the rapid F-T test in accordance with ASTM C666 Procedure A (2015), which is designed to evaluate the potential frost resistance of concrete in cold climates. The temperature range of 0° to 40°F was considered in the F-T cycles, and the cycle frequency was about 6 to 9 F-T cycles per day. The condition chamber used in the project is shown in Figure 3.5. Three samples were conditioned in the

chamber as the “conditioned group,” and another three were soaked in water as the “control group.”



Figure 3.5 Freeze-thaw conditioning machine

3.4.2 Dynamic modulus test

The dynamic modulus of concrete prism samples under different F-T conditioning cycles at every 30 cycles was evaluated using the transverse frequency test, in parallel with monitoring and assessment of UHPC material performance by smart aggregates. The dynamic modulus test is an impact test method that measures transverse frequency using either an accelerometer or a piezoelectric sensor attached to one end of the beam. The relative dynamic modulus is then computed using the fundamental transverse frequencies at 0 cycle and after a certain number of F-T cycles. The test setup for dynamic modulus measurement is shown in Figure 3.6. The dynamic modulus of the concrete beam samples at different cycles (up to 300 F-T cycles) was compiled and compared. A decrease of the dynamic modulus over accelerated F-T cyclic

conditioning indicates the degradation of concrete materials. For example, it is not recommended that a sample continue being tested after its relative dynamic modulus of elasticity has fallen below 60%.

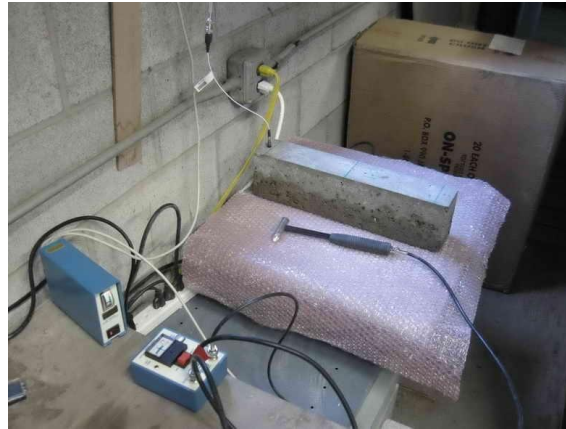


Figure 3.6 Dynamic modulus test setup at WSU

3.4.3 Smart aggregates

The ceramic piezoelectric (so-called PZT – lead zirconate titanate) patch is cast with a cement and sand mix to form a cementing module (known as smart aggregate) whose size and shape are similar to coarse aggregate, but which has the functionality of sensors and actuators. The fabrication process is illustrated in Figure 3.7.

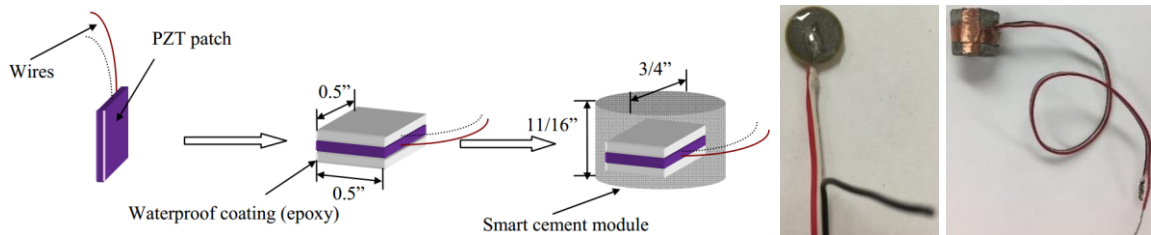


Figure 3.7 Fabrication process of smart aggregate

Embedded smart aggregates are capable of in situ exciting and receiving of elastic waves, from which the elastic properties, such as the wave modulus (such as the shear modulus), based on wave propagation, can be measured at any given F-T conditioning cycle for monitoring long-

term performance as well as for monitoring the strength growth of hardened concrete. Prismatic UHPC samples with dimensions of $3 \times 4 \times 16$ inches were cased with two embedded smart aggregates: one as an actuator and the other as the sensor (Figure 3.8). The samples were then subjected to F-T conditioning cycles after initial curing.

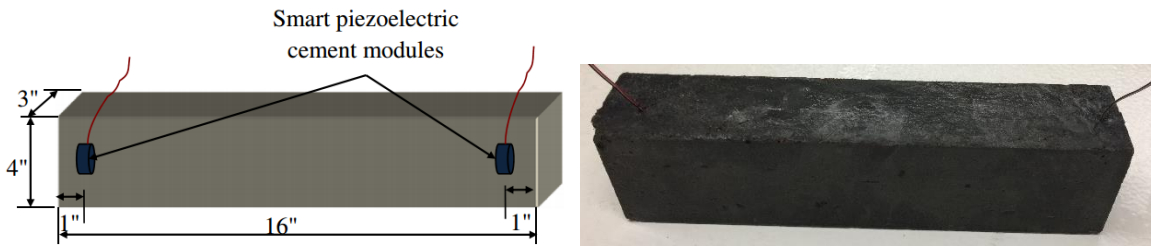


Figure 3.8 UHPC specimen with embedded smart aggregates

In order to detect damage inside the concrete, a 3.5-cycle 100 kHz sine wave package is excited through the actuator and windowed by a Hanning window; the response signal is captured by the sensor (Figure 3.9a). Figure 3.9b shows typical input and output wave signals. Both signals are exported as .txt files through a software program, Agilent IntuiLink Data Capture. The time of flight (TOF) of the wave package can be easily identified by the time interval between the peaks of the input signal and the first package of the output signal.

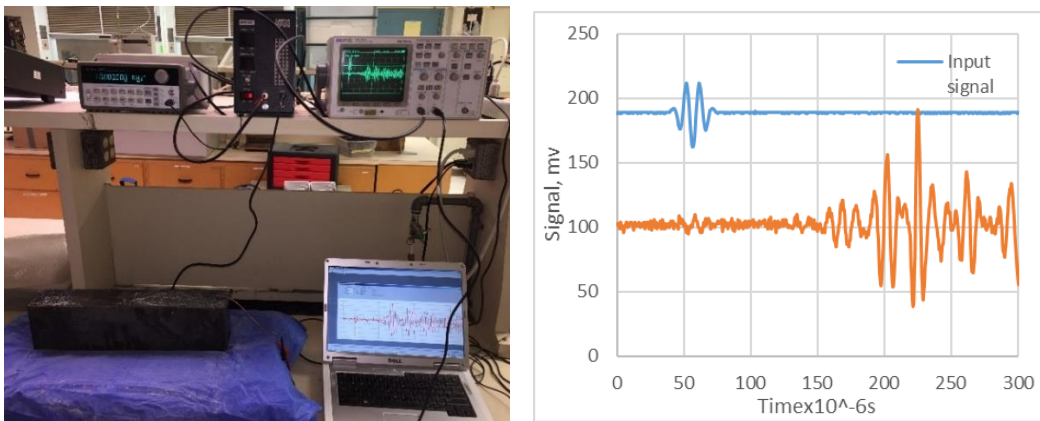


Figure 3.9 Wave modulus test setup and typical input and outputs signal

The wave elastic and shear modulus can be calculated from the TOF, as expressed in Equation 3.1.

$$\begin{aligned}E_{wave} &= 2(1 + \nu)\rho C_s^2 \\G_{wave} &= \rho C_s^2 \\C_s &= \frac{l}{TOF}\end{aligned}\tag{3.1}$$

where ρ and ν are the density and Poisson's ratio of concrete, and l is the distance between the actuator and the sensor.

3.4.4 X-ray CT imaging analysis

X-ray computed tomography (CT) was used to investigate the microstructural damage in UHPC under different F-T conditioning cycles. It was anticipated that as the F-T conditioning cycles increased, damage accumulation in the form of microcracks would be augmented. Internal damage can be detected under macroscale resolution, while the heterogeneous spatial distribution of porosity in concrete is characterized under microscale resolution. Eventually, the pore volume, pore size, and pore distribution can be virtually reconstructed using three-dimensional software (Simpleware). The X-ray CT test of conditioned UHPC samples was conducted at the University of California Irvine (UCI) using the Xradia 410 Versa X-ray microscope (Figure 3.10).

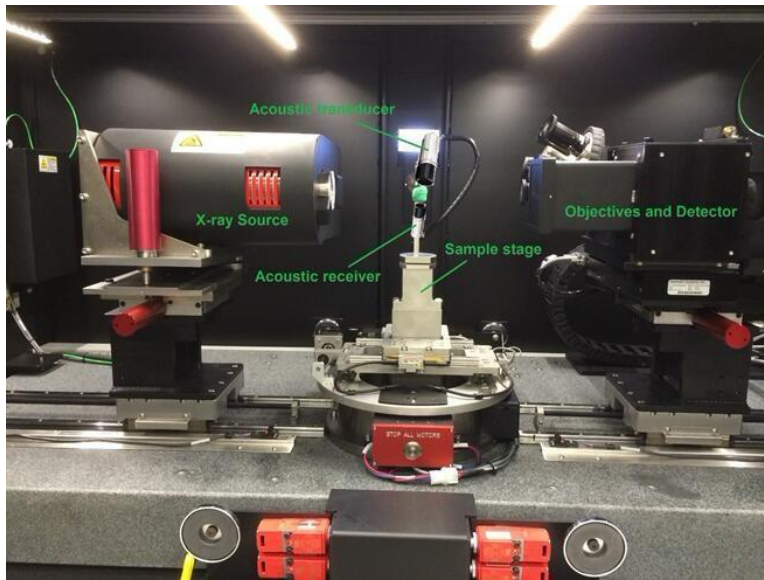


Figure 3.10 Xradia 410 Versa X-ray microscope at UCI

CHAPTER 4. TEST RESULTS AND ANALYSIS

In this chapter, results from the experimental tests conducted on UHPC specimens are presented and analyzed.

4.1 Results of Fresh and Hardened UHPC

4.1.1 Flow tests

The flow tests were conducted immediately to evaluate workability after mixing fresh UHPC. Initially, 12 mix designs (see Table 3.1) with different w/cm ratios, silica fume and cement contents, and HRWRA dosages were tested for their workability. Primarily based on its workability and compressive strength, C3, with a spread diameter of more than 8 inches, was selected for further mechanical property testing. The average flow of mixture C3 is approximately 9.5 inches in diameter, indicating that it is more like self-consolidated concrete.

4.1.2 Compressive strength and modulus of elasticity

The compressive strength and modulus of elasticity for mixture C3 were measured at 7 days, 14 days, and 28 days to study age-dependent compressive behaviors. In addition, different geometries of the specimen (2-inch cubes, 4-inch cubes, 3-inch \times 6-inch cylinders, and 4-inch \times 8-inch cylinders) were chosen to evaluate the effects of geometry on compressive strength. Similarly, the 4-inch \times 8-inch cylinders and the 6-inch \times 12-inch cylinders were comparably studied for modulus of elasticity. Three replicates were tested for all tests.

4.1.2.1 Size effects on compressive strength

The compressive strength of the 2-inch cubes was considered the reference parameter (benchmark). Figure 4.1 plots the averaged test data for the compressive strength of mixture C3

and the corresponding compressive strength at the reference age of 28 days: 16.01 ksi with a standard deviation of 0.97 ksi. The figure shows that the compressive strength of UHPC increased rapidly after casting, and that approximately 75% and 90% of compressive strength at 28 days was achieved after curing of 7 days and 14 days, respectively.

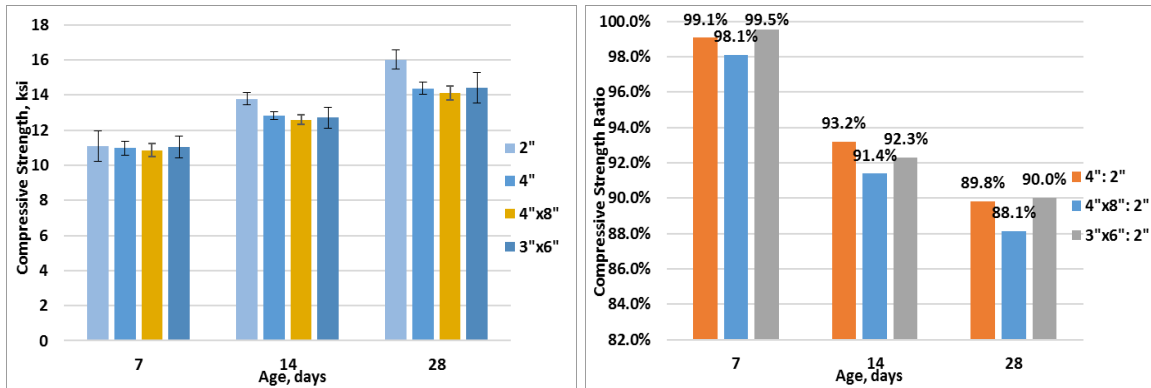


Figure 4.1 Compressive strengths at different ages and by different size specimens

The geometry of testing specimens has a moderate effect on the compressive strength of UHPC. Again, the compressive strength of 2-inch cubes was set as the reference data. Observe that the 2-inch cubes exhibited greatest compressive strength, followed by 3-inch \times 6-inch cylinders, while the compressive strengths of 4-inch cubes were almost the same as those of 4-inch \times 8-inch cylinders. The smaller-sized specimens usually showed higher compressive strength than the larger specimens. A possible reason for this difference could be that it takes more time for water absorption or diffusion inside larger specimens, which is related to the hydration of cementitious materials of UHPC. Another reason could be that the concrete is composed of elements of variable strength, and when concrete in large volume is subjected to uniform stress, it more likely contains a weaker element, leading to lower strength and early failure.

Figure 4.1 also shows that smaller samples (compared to their counterparts, e.g., 2-inch vs. 4-inch cubes, and 3-inch \times 6-inch vs. 4-inch \times 8-inch cylinders) usually have a larger

standard deviation because it is relatively difficult for air bubbles inside UHPC to come to the surface during vibration. Similar phenomena were observed by Orgass and Klug (2004) and Graybeal (2006).

4.1.2.2 Modulus of elasticity

The average modulus of elasticity of mixture C3 is illustrated in Figure 4.2. The modulus of elasticity was approximately 5,000 ksi at the reference age of 28 days, and the growth rate of the modulus of elasticity was faster than that of compressive strength; that is, approximately 88% and 92% at 28 days were achieved after curing of 7 days and 14 days, respectively. In addition, smaller specimens (4-inch × 8-inch cylinders) had a higher modulus of elasticity and lower standard deviation than larger specimens (6-inch × 12-inch cylinders).

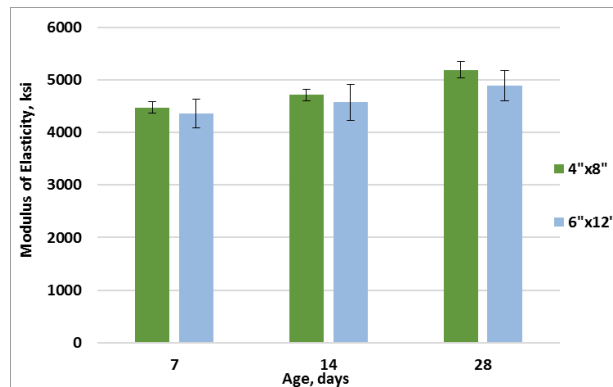


Figure 4.2 Modulus of elasticity at different ages and by different size specimens

4.1.2.3 Relationship between modulus of elasticity and compressive strength

The modulus of elasticity of concrete generally shows some correlation with the compressive strength of concrete. The ACI committee 318 (2014) provides one of the most widely used relationships for normal concrete; that is, the modulus of elasticity is equal to a constant multiplied by the square root of the compressive strength, which can be expressed by

$$E = \alpha\sqrt{f'_c} \quad (4.1)$$

where E is modulus of elasticity, ksi; f'_c is compressive strength, psi; and α is scale factor.

To establish empirical relationships between the modulus of elasticity and compressive strength, the compressive strength based on 3-inch \times 6-inch cylinders and the modulus of elasticity based on 4-inch \times 8-inch cylinders were tested up to 90 days. Then the scalar factor in Eq. (4.1) was determined using the least squares method, resulting in $\alpha = 43,500$. As shown in Figure 4.3, the modulus of elasticity prediction equation can accurately fit the curve from the experimental results. However, due to greater compressive strength of UHPC, the scale factor is smaller than that of conventional concrete of normal weight ($\alpha = 57,000$).

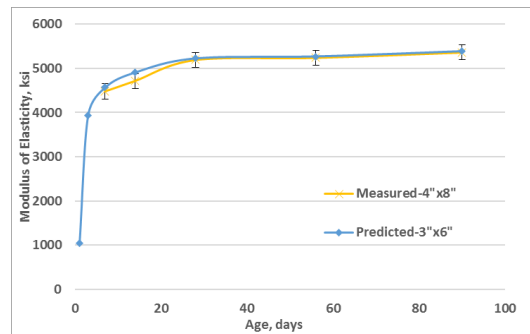


Figure 4.3 Measured and predicted modulus of elasticity

4.1.3 Tensile strength

Three test methods were employed to measure the tensile strength-associated properties of UHPC: (1) flexural prisms with dimensions of 3 \times 4 \times 16 inches, (2) splitting cylinders of 6-inch \times 12-inch, and (3) direct tensile dogbones with cross section of 2-inch \times 2-inch. Tensile strength tests were conducted at 7 days, 14 days, and 28 days to study tensile strength development over time. Figure 4.4 shows averaged testing results for flexural strength (MOR) from the bending test of flexural prisms, splitting tensile strength (IDT) from the splitting tension

test of cylinders, and direct tensile strength (DDT) from the tension test of the dogbone-shaped specimens; peak loads were used for the calculation.

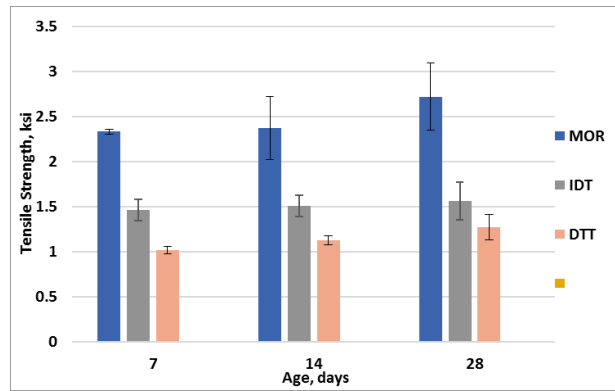


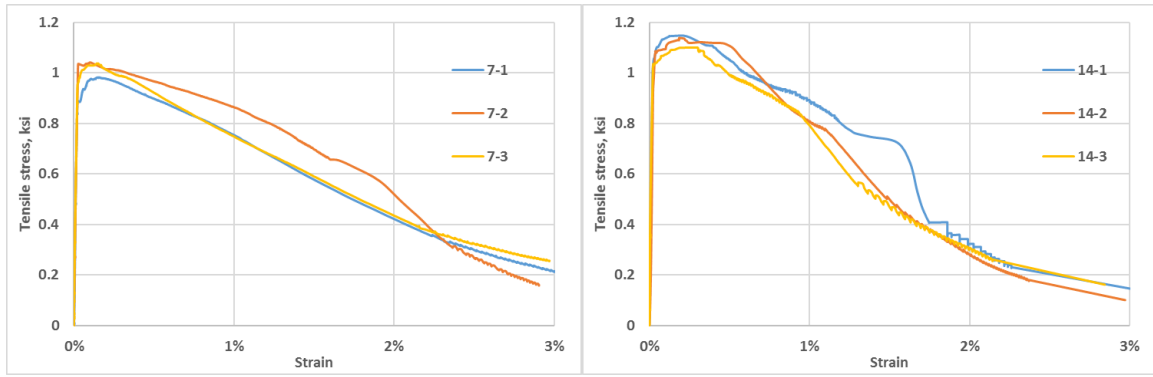
Figure 4.4 Comparison of tensile strength

The values indicated in Figure 4.4, though significantly different, are all much higher than the values of conventional concrete. Of the three different approaches for measuring tensile strength, the flexural strength test reported the greatest value (2.72 ksi at 28 days), followed by splitting tensile strength (1.56 ksi at 28 days) and direct tensile strength (1.27 ksi at 28 days). The significant difference in tensile strength values measured by these three test methods might be caused by overestimation of the tensile hardening response and different stress distributions and boundary conditions in the test specimens. In general, UHPC can exhibit sustained strain hardening and then reach greater tensile strength after first cracking. It has been observed that flexural beam and splitting cylinder-based test methods are more susceptible to overestimation of tensile load due to the tensile strength at peak load after post-cracking, which can be 3 times the tensile load at first cracking (Graybeal and Baby 2013).

Boundary conditions and load applications cause non-uniform tensile stress distribution in test specimens (e.g., linear stress distribution through the depth of the beam in the flexural beams, stress concentrations at the loading points, and non-uniform stress distribution in splitting cylinders). However, peak post-cracking tensile strength in the direct tension test was slightly

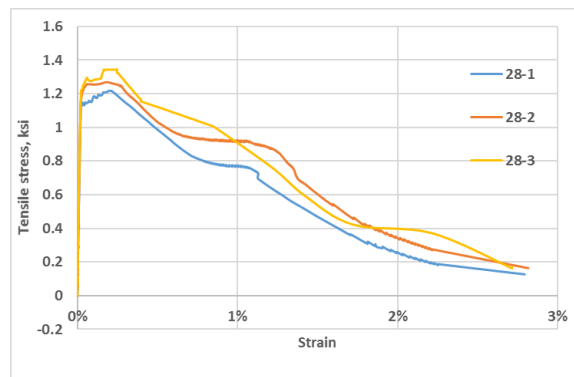
greater than that at the first cracking, and the tensile stress distribution in the cross section of direct tension was more uniform compared with that of both flexural beams and splitting cylinders. In addition, due to the limited tests conducted, the strain response in flexural beams and splitting cylinders was not measured, and the stress-strain curve and the tensile load at first cracking could not be observed.

In this study, direction tension tests were extensively performed to evaluate the tension strength of UHPC coupled with F-T conditioning. The average elongation displacement of two LVDTs with a gauge length of 6 inches was used to calculate the responding tensile strain at the middle of the specimens in the direct tension tests. The longer gauge length was used for capturing and measuring the stress-strain data, because the probability of first and ultimate cracking occurring within the gauge length is higher. Figure 4.5 shows the stress-strain relationship curves in the direct tension tests at different testing age. Note that the stress-strain response and the failure mode of UHPC in direct tension were quite different from those of conventional concrete. The UHPC exhibited excellent ductile behavior, with a gradual decline in stress versus strain due to the reinforcement of steel fibers. This ductile response can be divided into three phases. Phase I is the linear elastic behavior, which is from initial load application until the first crack occurs. Phase II shows no stress falling branch and multiple cracks from strain hardening. In Phase III, after the onset of cracks, gradual decrease in the stress versus the strain due to pullout of steel fibers occurs, showing stress-crack opening behavior (strain softening). The strain at the first crack ranged from 0.015% to 0.03%, but it showed no clear relationship with the age of curing at the time of testing. Post-cracking occurred near the strain of 0.2%. The UHPC could even possess 0.2 ksi tensile stress when the tensile strain reached 3%.



(a) 7 days

(b) 14 days



(c) 28 days

Figure 4.5 Stress-strain response of UHPC in direct tension with different ages of curing

An alternative method to obtain the modulus of elasticity is to find the slope of elastic phase from the stress-strain relationship curves obtained from the direct tension test. The comparison of the modulus of elasticity with the results from the compression tests is shown in Figure 4.6. The maximum difference between the modulus of elasticity values obtained from the direct tension and cylinder compression tests is approximately 5%.

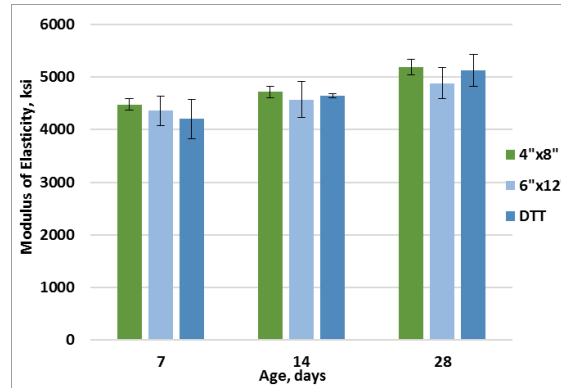
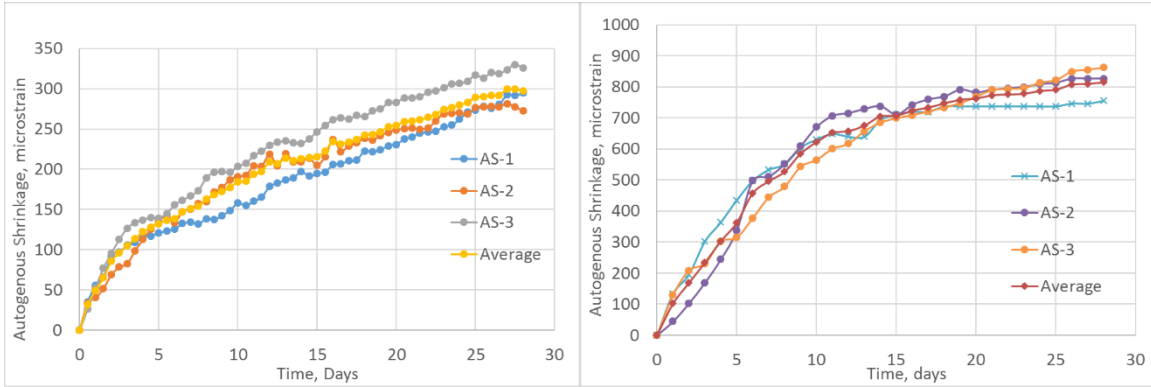


Figure 4.6 Comparisons of modulus of elasticity from the compression and direct tension tests

4.1.4 Shrinkage

Shrinkage of unstrained UHPC prismatic specimens was measured from demolding until 28 days. Prismatic specimens in sizes of $1 \times 1 \times 11.25$ inches and $4 \times 4 \times 11.25$ inches were used to investigate size (specific surface to volume ratio) effects on shrinkage. All prisms were stored, and initial lengths were measured in a climate-controlled room with a temperature of $73 \pm 3^\circ\text{F}$ ($23 \pm 2^\circ\text{C}$) and relative humidity of $50 \pm 4\%$. Surface treatment was the only difference between the specimens: sealed surface for autogenous shrinkage and unsealed for free shrinkage.

Figure 4.7 depicts the autogenous shrinkage behavior of UHPC specimens up to 28 days after demolding. The cross section size of prisms has a great effect on the autogenous shrinkage behavior of UHPC due to different moisture diffusion distances, and the 1-inch prisms showed greater autogenous shrinkage and a higher shrinkage rate than the 4-inch prisms. It should be mentioned here that from the inherent relationship among hydration of cementitious materials, autogenous shrinkage, and strength growth, in terms of the shrinkage measurement, the 4-inch prisms were more representative and consistently matched the strength gain rate better than the 1-inch slimmer prisms.

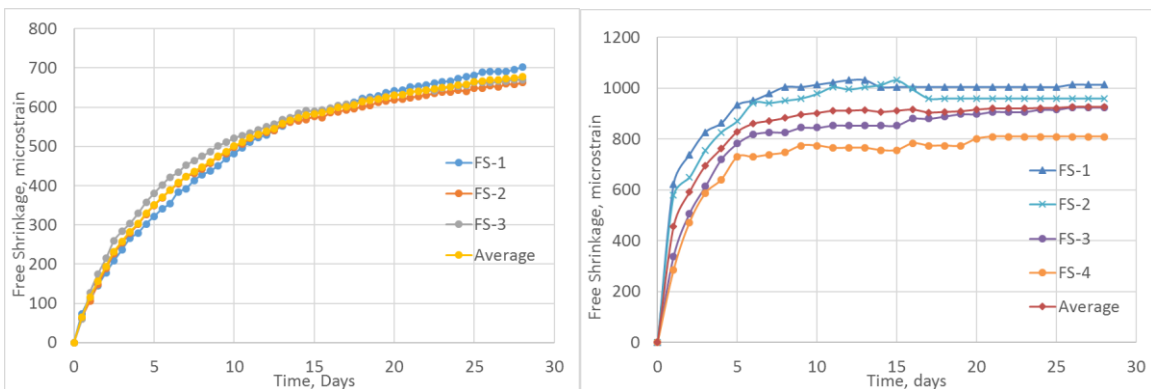


(a) Autogenous shrinkage, 4-inch prisms

(b) Autogenous shrinkage, 1-inch prisms

Figure 4.7 Comparison of autogenous shrinkage

Figure 4.8 provides the free shrinkage of UHPC mixtures up to 28 days after demolding. Free shrinkage mainly consists of both autogenous shrinkage and drying shrinkage. After 28 days of exposure to 50% relative humidity, the average shrinkage value was 678 microstrains. It can be seen in Figure 4.8 that the free shrinkage behavior showed a similar trend of autogenous shrinkage, and the 4-inch prisms showed much less and slower free shrinkage than the 1-inch prisms. Approximately 90% of free shrinkage for the 1-inch prisms occurred within the first 7 days.



(a) Free shrinkage, 4-inch prisms

(b) Free shrinkage, 1-inch prisms

Figure 4.8 Comparison of free shrinkage

Figure 4.9 depicts the testing results of restrained shrinkage performed on mixture C3 used in this study, and it shows the measured steel strains in the restrained ring specimens. No sudden jump (usually happens in case of conventional concrete within 28 days) is observed in these shrinkage strain curves, indicating that no shrinkage-induced cracking occurred in the UHPC ring due to its high tensile strength with strong fiber reinforcement.

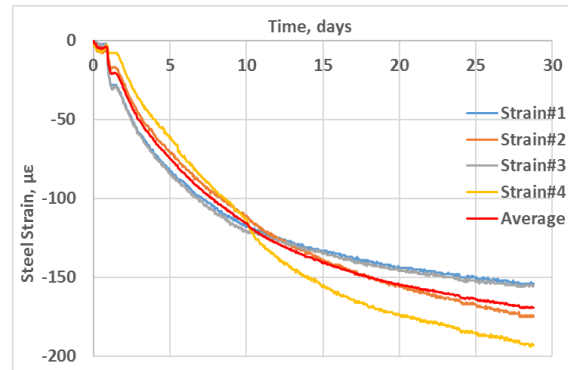


Figure 4.9 Restrained shrinkage from ring tests

4.2 Test Results of Durability Study

4.2.1 Dynamic modulus and wave modulus

The vibration-based dynamic modulus (E_{dyn}) test using an impact hammer and the wave propagation-based wave modulus (E_{wave}) test using embedded smart aggregates were simultaneously conducted on the control groups of UHPC beams during the curing period up to 90 days. The variances of the average modulus of elasticity (from the compressive test), dynamic modulus, and wave modulus with respect to the curing age are comparatively illustrated in Figure 4.10. It can be seen from Figure 4.10 that the modulus of elasticity obtained from all the test methods (compression, hammer vibration, and wave propagation) gradually increases with the increase of curing time, indicating that the samples are gradually gaining stiffness and strength. The modulus of elasticity of concrete is influenced by the loading rate. Among these testing methods, the modulus of elasticity by compressive test is obtained under quasi-static

loading, the dynamic modulus is measured based on low frequency (1~10 kHz), and the wave modulus is measured based on wave propagation under high frequency (100 kHz in this study). The testing results coincide with this relationship between modulus and load rate; that is, the wave modulus is slightly higher than the dynamic modulus, and the modulus of elasticity (MOE) from the compressive test is lowest.

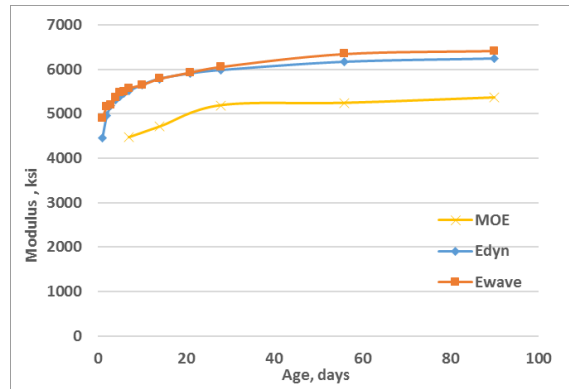


Figure 4.10 Comparison of values of modulus of elasticity by different test methods

In parallel, the aforementioned two non-destructive monitoring techniques, that is, the vibration-based dynamic modulus (E_{dyn}) test and the wave propagation-based wave modulus (E_{wave}) test were simultaneously conducted on UHPC beams at different freeze-thaw (F-T) conditioning cycles. In the meantime, the control groups of UHPC beams continued to be kept under lime-saturated water. The variances of the average dynamic modulus and wave modulus with respect to the curing cycles are comparatively illustrated in Figure 4.11. The UHPC beams were conditioned up to 600 F-T cycles due to the time limit. As seen in Figure 4.11, both the dynamic modulus and wave modulus values increase instead of decreasing, with the increase of F-T cycles, which is different from normal concrete but a similar finding reported in others' conclusions (Graybeal and Hartmann 2003; Shaheen and Shrive 2006), indicating that UHPC exhibits excellent frost resistance at the first 600 cycles. The maximum increased ratios of dynamic modulus and wave modulus values with F-T conditioning are 5.2% and 6.4%,

respectively. In comparison, the maximum increased ratios of dynamic modulus and wave modulus values in the control groups are 13.9% and 16.1%, respectively. Both the wave modulus values and the corresponding increasing ratios are larger than those based on the dynamic modulus, which indicates that the wave propagation-based method is more sensitive than the vibration-based method. Two possible reasons are considered to explain the difference: (1) the cement hydration with an external moisture supply outpaces the frost damage; (2) the cement hydration slows down at lower temperatures. Thus, in future study, experimental evaluation tests will be conducted on UHPC beams with more F-T cycles (up to 1,500 cycles), and microstructure study on conditioned UHPC will be conducted to reveal the frost damage-forming mechanism.

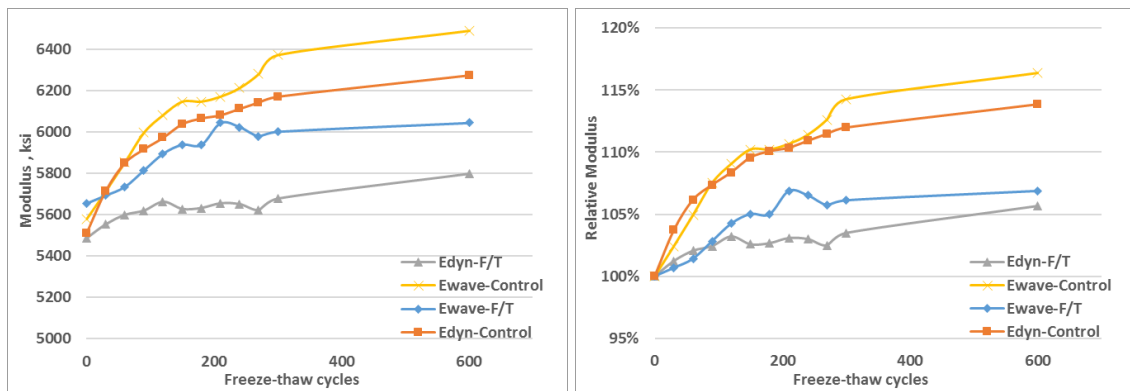


Figure 4.11 Comparison of dynamic and wave modulus values and their relative modulus

The surface scaling of UHPC samples at 0, 180, 300, and 600 cycles is illustrated in Figure 4.12. Few tiny scaling spots are observed on the sample surfaces after 600 cycles due to the dense microstructure of UHPC; thus, the effects of surface scaling are negligible.

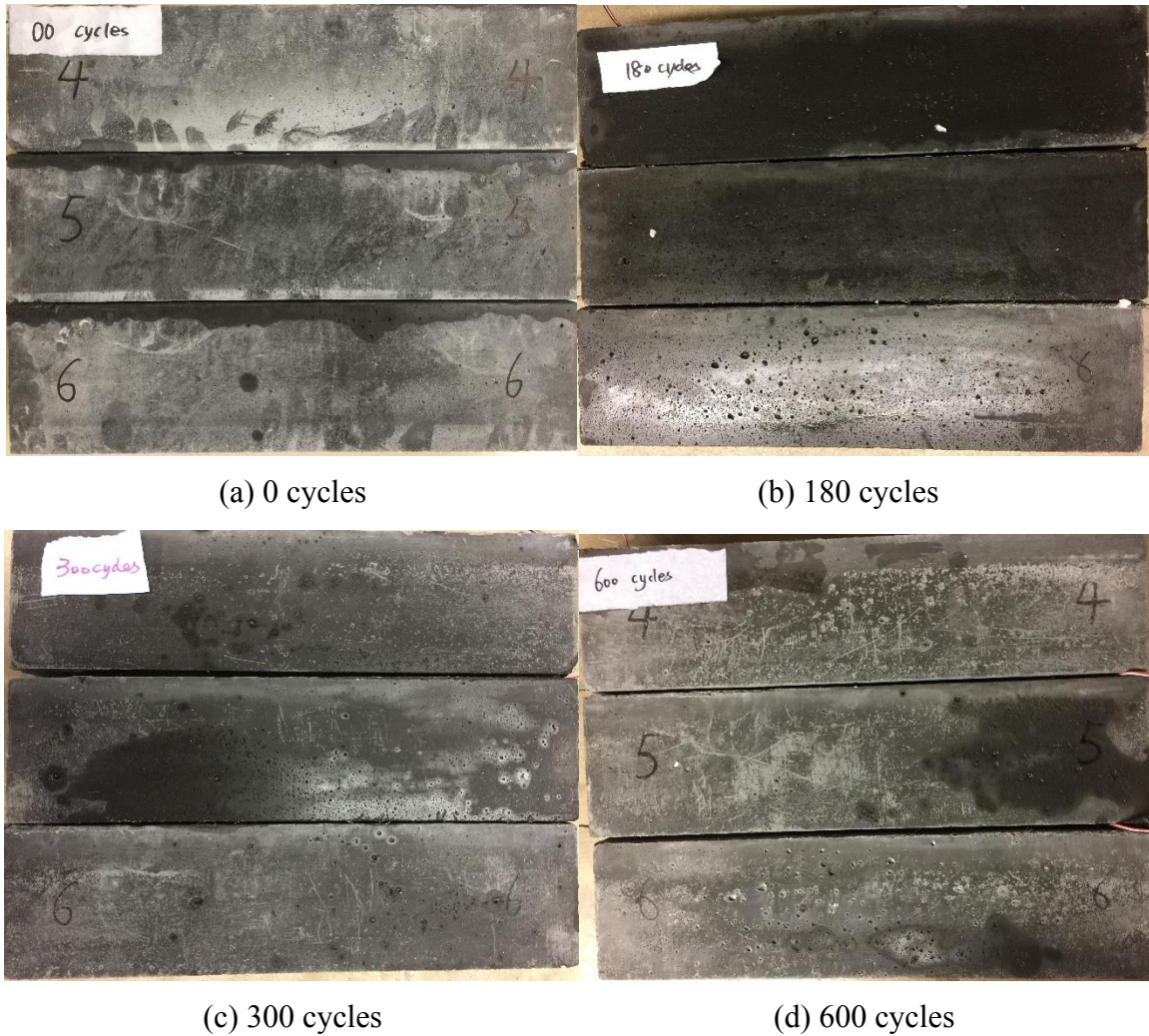


Figure 4.12 Comparison of surface scaling of UHPC at different F-T cycles

4.2.2 Results from direct tension test

Direct tension tests were conducted on UHPC dogbone-shaped specimens at 150 and 300 conditioning cycles to evaluate F-T effects on tensile strength as well as on the stress-strain relationship. Three replicates were tested at each F-T conditioning cycle. The variances of the average tensile strength and modulus of elasticity with respect to the curing cycles are comparatively illustrated in Figure 4.13. Note in Figure 4.13 that both the tensile strength and the modulus of elasticity increase slightly during the F-T process, and at 300 F-T cycles, the specimens gain approximately 2% and 7.1% in tensile strength and modulus of elasticity,

respectively, which is consistent with the increases of dynamic and wave moduli with respect to F-T conditioning cycles.

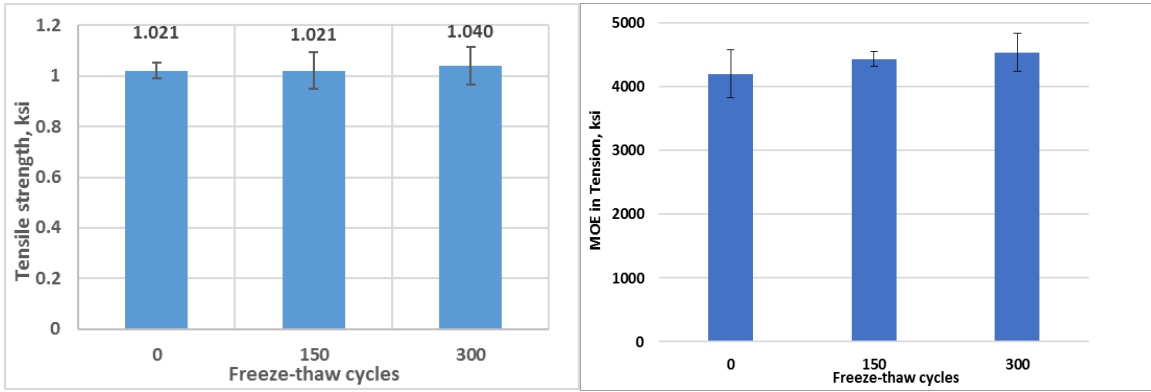
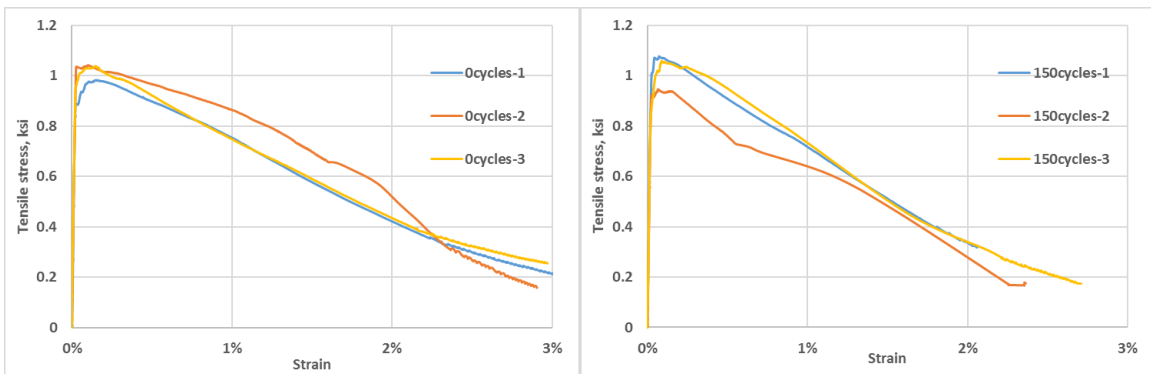


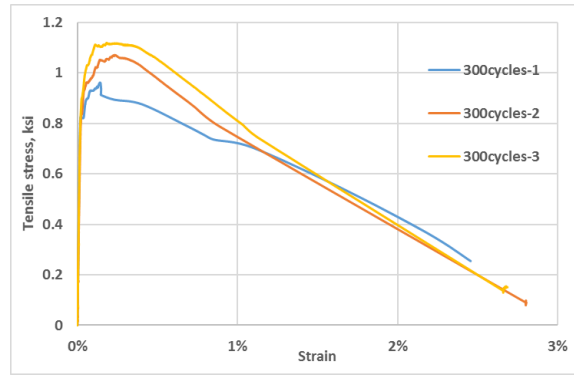
Figure 4.13 Tensile strength and modulus of elasticity from direct tension test at different F-T cycles

Figure 4.14 comparatively depicts the stress-strain relationship curves in tension at 0, 150, and 300 F-T cycles. No obvious differences in strain hardening and ductility could be found. The direct tension tests will be continuously conducted on UHPC specimens with more F-T action.



(a) 0 cycles

(b) 150 cycles



(c) 300 cycles

Figure 4.14 Stress-strain response of conditioning UHPC in direct tension

4.2.3 X-ray CT imaging analysis

Modulus of elasticity and strength-based evaluation methods are not capable of revealing microstructural damage in UHPC under F-T action. To characterize the material degradation of UHPC caused by frost action, internal damage evolution, porosity, pore structure, and fiber distributions were investigated using an X-ray CT machine. Specimens of UHPC with the dimensions of $14.57 \times 14.57 \times 14.57$ mm were used to investigate internal damage accumulation during different F-T cycles. Two-dimensional (2D) X-ray radiographs were first collected at many viewing angles and then virtually reconstructed, based on the inner density distribution of the radiographs. One 2D image can be reconstructed from each scanning. One thousand slices were scanned for each sample and then reconstructed to generate a three-dimensional (3D) image through Simpleware software. The reconstructed 3D images can be segmented to separate pores and steel fibers from the matrix to obtain the results of porosity, pores, and steel fiber distribution. Figure 4.15 shows typical 2D and 3D images of UHPC with 300 F-T cycles. No obvious cracks or fractures were detected in these images. Three material constituents inside UHPC can be clearly distinguished after reconstruction: concrete matrix (gray), steel fibers (white spots), and air voids (dark spots).

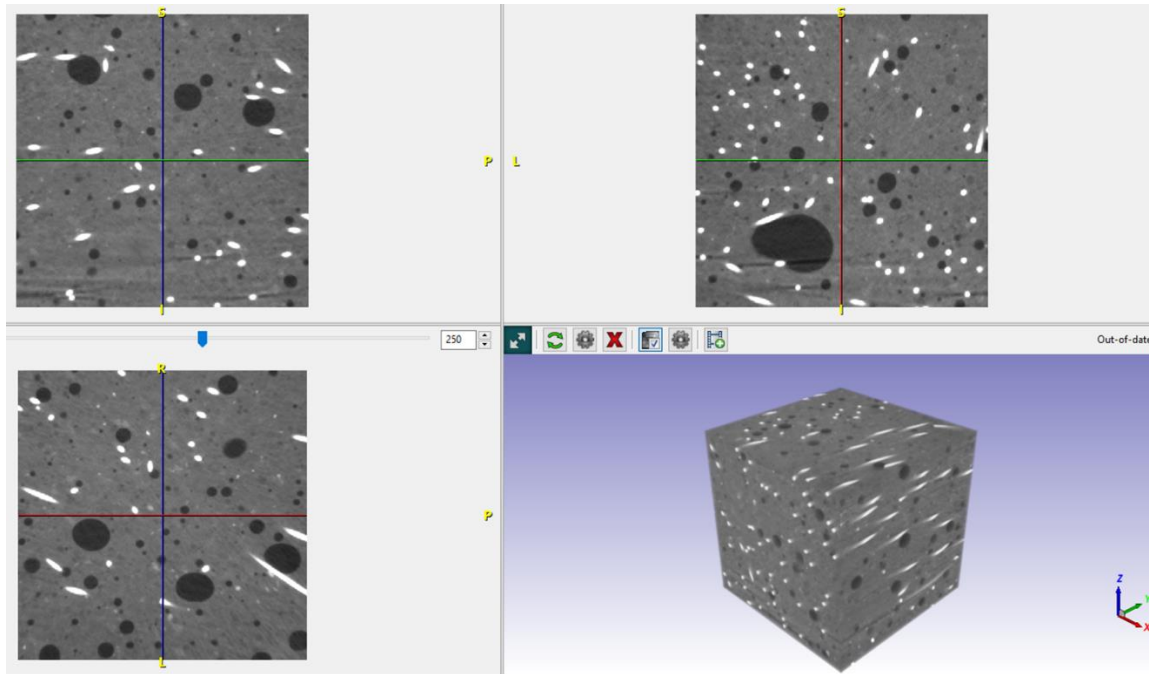


Figure 4.15 2D and 3D reconstructed slices of UHPC
(concrete matrix, gray; steel fibers, white spots; air voids, dark spots)

Three-dimensional imaging analysis and quantitative measurements that focused on the pore structure, including porosity, pore volume, surface area, and pore size distribution, were performed on UHPC with different F-T cycles. Figures 4.16 and 4.17 illustrate the void and steel fiber distribution in UHPC at different cycles. The test data obtained from reconstruction using X-ray CT are shown in Table 4.1. Although no obvious damages occur on UHPC, the frost impact on the internal micropores is still notable. The porosity, pore volume, and surface area correspondingly increase with the increase of freeze cycles. When F-T reached 300 cycles, the porosity, pore volume, and surface area increased 45.7%, 46.1%, 10.2%, respectively. The volume of steel fiber in UHPC ranged from 2.07 to 2.11, which is very close to the design percentage of UHPC used in the mix.

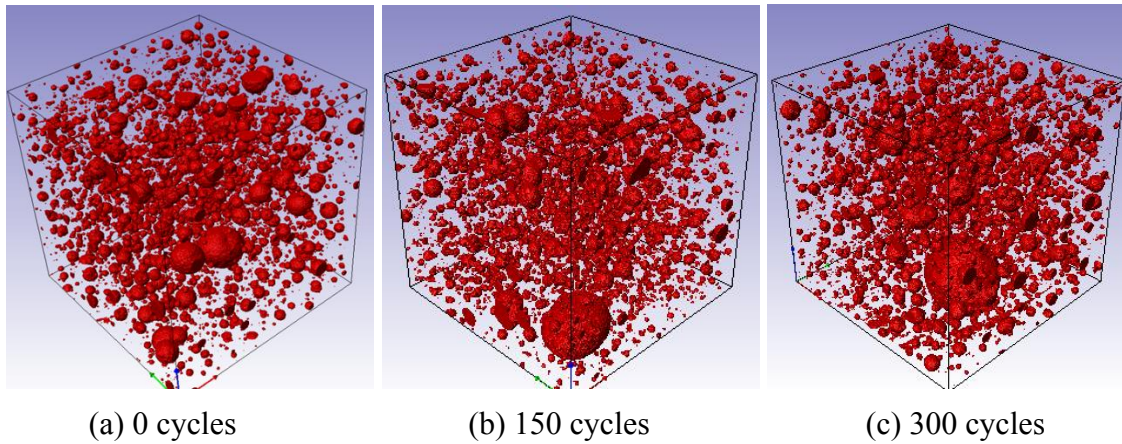


Figure 4.16 Segmented pores in UHPC at different F-T cycles

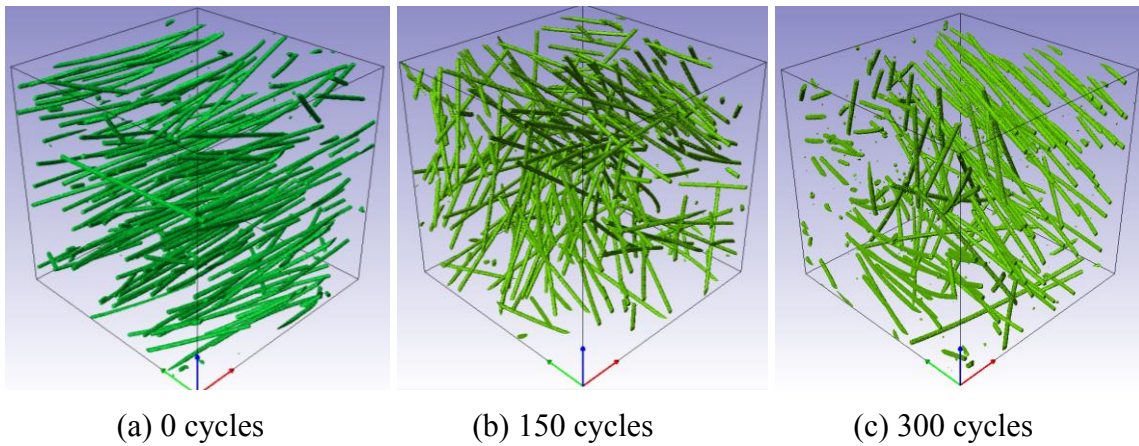


Figure 4.17 Segmented steel fibers in UHPC at different F-T cycles

Table 4.1 Pore and fiber information in UPHC

Number of F-T cycles	Porosity, %	Pore volume, mm ³	Pore surface area, mm ²	Steel fiber volume fraction, %
0	4.62	141	1502	2.11
150	4.61	140	1510	2.08
300	6.73	206	1655	2.07

Both porosity and pore distribution in UHPC significantly affect its long-term durability.

The porosity deterioration of UHPC under frost attack eventually leads to internal damage of the

concrete. Three ranges of pore size are considered in calculating the pore distribution: 0.01–0.1 mm, 0.1–1.0 mm, and 0.1+ mm. Pores larger than 1 mm mainly contribute to porosity incensement and are more likely to affect the properties of UHPC under F-T cycles. Figure 4.18 depicts the histograms of pore size distribution under different F-T cycles. The pore size above 1 mm distribution is emphasized in Figure 4.19. The results of pore distribution analysis show that most of the pore sizes in UHPC at 0, 150, and 300 F-T cycles fall in the range of 0.01–0.1 mm and 0.1+ mm. The pore size 0.1+ mm obviously increases approximately 100% after 300 F-T cycles. Again, due to limited tests on UHPC samples with limited curing cycles, damage evolution and accumulation in terms of pore-size increase due to frost attack are still not manifested. More microscopic observations and X-ray CT image analysis of UHPC samples with increased F-T conditioning cycles will be conducted.

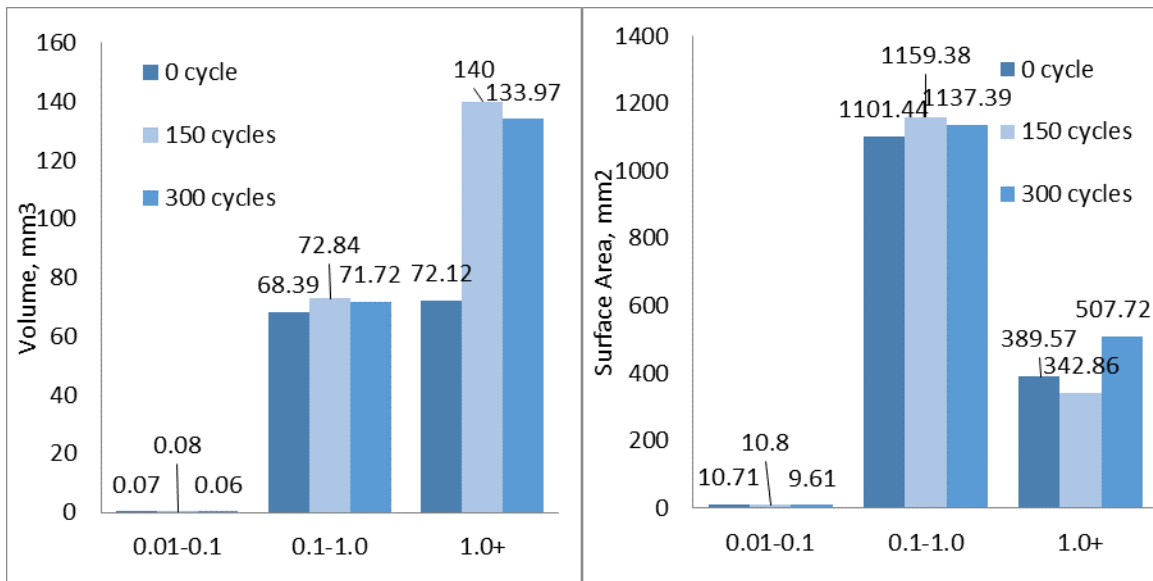


Figure 4.18 Pore distribution in UHPC at different cycles

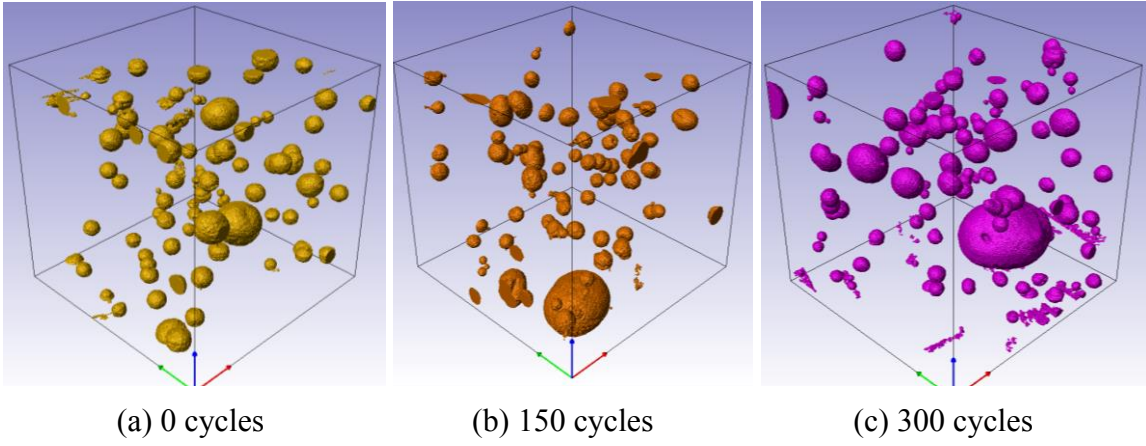


Figure 4.19 Pore size above 1 mm in UHPC at different cycles

CHAPTER 5. CONCLUSIONS AND RECOMMENDATIONS

5.1 Summary

This study, in conjunction with a related study by the Washington State Department of Transportation (WSDOT) (Qiao et al. 2017), developed and characterized a cost-effective ultra-high performance concrete (UHPC) that is resilient in cold climates. The concrete's durability in cold regions was investigated using accelerated freeze-thaw (F-T) conditioning and smart sensor technology. A comprehensive review of the literature on UHPC was first conducted. Twelve UHPC mixtures were developed using locally available materials, from which one viable UHPC mixture (i.e., C3) was selected for further evaluation of its durability based on the recommendations of the related WSDOT project (Qiao et al. 2017). The following findings are based on the experimental evaluation of UHPC mixtures.

5.2 Findings

1. Based on the extended literature review and available UHPC mixtures, locally available sand, cement, and admixtures as well as domestic steel fibers that produce cost-effective UHPC were identified. More importantly, expensive materials, such as quartz powder, imported fibers, and thermal and pressure treatments, commonly used in commercial products and other studies, were not used. Based on adequate workability (i.e., a flow spread of 9.5 inches in diameter) and mechanical tests, one optimal mixture—C3—was found relatively stronger and thus was selected for further experimental evaluation.

2. Following the standard test procedures for concrete and cementitious material characterization, test methods for both the fresh and hardened properties of UHPC were selected. The tensile strength-related properties and tests of UHPC were particularly emphasized. The

direct tension test is capable of obtaining the tensile stress-strain behavior of the specimens, from which the ductility of UHPC is characterized.

3. The optimal mixture C3 performs a compressive strength of 15 ksi, direct tensile strength of 1.27 ksi, elastic modulus of 5,000 ksi, and shrinkage of 630 $\mu\epsilon$ at 28 days, characteristics that are comparable to those of commercial products and other studies. The strength, modulus of elasticity, and ductility of C3 all outweigh those of conventional concrete.

4. Standard and non-standard test procedures for evaluation of concrete under freeze-thaw attack were simultaneously conducted. The wave propagation-based health monitoring technique (material property assessment) using embedded smart aggregates is capable of assessing the strength growth and material degradation process in UHPC. X-ray CT imaging analysis is capable of investigating the microstructure of UHPC, where porosity deterioration can be observed under freeze-thaw attack.

5. When reaching 300 freeze-thaw cycles, the strength and modulus of elasticity in tension, dynamic modulus, and wave modulus show a slight increase from the virgin samples at 0 freeze-thaw condition cycle, indicating that UHPC should have excellent frost resistance in cold climates. No internal damage (cracks or fractures) was found from X-ray imaging analysis up to 300 cycles; however, the porosity deterioration observed in the freeze-thaw conditioning process, indicating internal damage to the UHPC, would more likely have occurred if freeze-thaw conditioning had continued. All durability-related tests indicate that the proposed/developed UHPC mix is resilient to and robust in freeze-thaw action and is suitable for application in cold climates.

In summary, one optimal UHPC mixture, containing locally available materials, and its related mechanical properties and durability performance were evaluated. The strength, modulus

of elasticity, and frost resistance of the UHPC mixture were found superior to those of conventional concrete and comparable to commercially available UHPC. The material property assessment by embedded smart aggregates and X-ray CT imaging analysis are effective for investigating the potential damage evolution in UHPC under accelerated freeze-thaw conditioning.

5.3 Recommendations

The results reported here are based on a limited study (up to 300 freeze-thaw conditioning cycles) of long-term durability performance in cold climates and a material property assessment of a UHPC mixture produced using locally obtained materials. Based on the experimental program conducted, the following recommendations are made for improved understanding of the long-term performance of UHPC in cold climates:

1. Due to the time duration of this project (just 1 year), limited freeze-thaw conditioning cycles were conducted on UHPC. It is important that the performance (strength, modulus of elasticity, ductility, porosity, etc.) of UHPC with longer freeze-thaw action be tested, since UHPC is expected to have a longer service life than conventional concrete. On the other hand, to accelerate the aging process, a more severe freeze-thaw conditioning protocol is needed to condition the samples at a faster rate so that deterioration or degradation of the UHPC can be observed with reduced conditioning time.

2. Once the degradation of material properties is experimentally evaluated, damage mechanics-based models hold the potential of evaluating damage accumulation and the failure mechanism of UHPC under frost attack and predicting long-term material deterioration and service life.

3. It has been established that UHPC exhibits superior resistance to rapid freeze-thaw action. However, salty deicers are commonly used in cold regions to melt snow and ice for improved traffic safety, and the resistance of UHPC under combined frost and chemical attacks should be investigated, because the corrosion of steel fibers and the effects on UHPC performance cannot be neglected.

4. The innovative and effective smart aggregate technique is capable of in situ monitoring strength growth, assessing long-term durability, and detecting potential damage in UHPC materials and structures.

REFERENCES

- AASHTO T334-08. (2012). “Standard method of test for estimating the cracking tendency of concrete.” American Association of State Highway and Transportation Officials, Washington, DC.
- ACI Committee 318 (2014). “Building code requirements for structural concrete (ACI 318-14); and commentary (ACI 318R-14).” American Concrete Institute, Farmington Hills, MI.
- Allena, S., and Newton, C. M. (2011). “Ultra-high strength concrete mixtures using local materials.” *Journal of Civil Engineering and Architecture*, 5(4), 322–330.
- Allena, S., Newton, C. M., and Tahat, M. N. (2012). “Mechanical Properties of Ultra-High Strength Concrete with Local Materials.” *Advances in Civil Engineering and Building Materials*, Chang, Al Bahar, and Zhao (Eds.), CRC Press, pp. 195–198.
- ASTM C1018-97 (Withdrawn 2006). “Standard test method for flexural toughness and first-crack strength of fiber-reinforced concrete (using beam with third-point loading).” ASTM International, West Conshohocken, PA.
- ASTM C109/C109M-16a (2016). “Standard test method for compressive strength of hydraulic cement mortars (Using 2-in. or [50-mm] cube specimens).” ASTM International, West Conshohocken, PA.
- ASTM C1231/C1231M-15 (2015). “Standard practice for use of unbonded caps in determination of compressive strength of hardened cylindrical concrete specimens.” ASTM International, West Conshohocken, PA.
- ASTM C128-15 (2015). “Standard test method for relative density (specific gravity) and absorption of fine aggregate.” ASTM International, West Conshohocken, PA.

ASTM C1437-15 (2015). “Standard test method for flow of hydraulic cement mortar.” ASTM International, West Conshohocken, PA.

ASTM C157/C157M-08 (2014). “Standard test method for length change of hardened hydraulic-cement mortar and concrete.” ASTM International, West Conshohocken, PA.

ASTM C192/C192M-16 (2016). “Standard practice for making and curing concrete test specimens in the laboratory.” ASTM International, West Conshohocken, PA.

ASTM C215-14 (2014). “Standard test method for fundamental transverse, longitudinal, and torsional resonant frequencies of concrete specimens.” ASTM International, West Conshohocken, PA.

ASTM C39/C39M-16 (2016). “Standard test method for compressive strength of cylindrical concrete specimens.” ASTM International, West Conshohocken, PA.

ASTM C469/C469M-14 (2014). “Standard test method for static modulus of elasticity and Poisson’s ratio of concrete in compression.” ASTM International, West Conshohocken, PA.

ASTM C496/C496M-11 (2011). “Standard test method for splitting tensile strength of cylindrical concrete specimens.” ASTM International, West Conshohocken, PA.

ASTM C617/C617M-15. (2015). “Standard practice for capping cylindrical concrete specimens.” ASTM International, West Conshohocken, PA.

ASTM C666/C666M-15 (2015). “Standard test method for resistance of concrete to rapid freezing and thawing.” ASTM International, West Conshohocken, PA.

ASTM C78/C78M-15b (2016). “Standard test method for flexural strength of concrete (using simple beam with third-point loading).” ASTM International, West Conshohocken, PA.

- Brooks, J. J., and Wainright, P. J. (1983) “Properties of ultra-high-strength concrete containing a superplasticizer.” *Magazine of Concrete Research*, 35(25), 205_213.
- Brooks, J. J., and Hynes, J. P., (1996). “Creep and shrinkage of ultra high-strength silica flume concrete.” *Creep and Shrinkage of Concrete*, Bazant, Z. P., Carol, I., and Spon, E. and F. N. (Eds.), London, pp. 493–498.
- Cahill, P., O'Keeffe, R., Jackson, N., Mathewson, A., and Pakrashi, V. (2014). “Structural health monitoring of reinforced concrete beam using piezoelectric energy harvesting system.” *EWSHM-7th European Workshop on Structural Health Monitoring*.
- Colleparidi, S., Coppola, L., Troli, R., et al. (1997). “Mechanical properties of modified reactive powder concrete”. *Proc., 5th CANMET/ACI International Conference on Superplasticizers and Other Chemical Admixtures in Concrete*, Rome, Italy, Publication No. SP-173, Malhotra V. M. (Ed.), American Concrete Institute, Farmington Hills, MI, pp. 1–21.
- Colleparidi, M. (2003). “A state-of-the-art review on delayed ettringite attack on concrete.” *Cement and Concrete Composites*, 25(4–5), 401–407.
- Diamond, S. (1996). “Delayed ettringite formation – Processes and problems.” *Cement and Concrete Composites*, 18(3), 205–215.
- Dili, A. S., and Santhanam, M. (2004). “Investigations on reactive powder concrete: A developing ultra high strength technology.” *The Indian Concrete Journal*, 78(4), 33–38.
- Eppers, S., and Muller, C. (2008). “Autogenous shrinkage strain of ultra-high-performance concrete (UHPC).” *Ultra High Performance Concrete (UHPC), Proc., 2nd International Symposium on Ultra High Performance Concrete*, Kassel, Germany, pp. 433–441.

- Graybeal B. A. (2006). "Material Property Characterization of Ultra-High Performance Concrete." U.S. Department of Transportation, Federal Highway Administration. Publication No. FHWA-HRT-06-103.
- Graybeal, B. A. (2007). "Compressive behavior of ultra-high performance fiber-reinforced concrete." *ACI Materials Journal*, 104(2), 146–152.
- Graybeal, B. A. (2015). "Compression testing of ultra-high-performance concrete." *Advances in Civil Engineering Materials*, 4(2), 102–112.
- Graybeal, B. A., and Hartmann, J. L. (2003). "Strength and durability of ultra-high performance concrete." *Concrete Bridge Conference*, pp. 1–20.
- Graybeal, B. A., and Baby, F. (2013). "Development of direct tension test method for ultra-high-performance fiber-reinforced concrete." *ACI Materials Journal*, 110(2), 177–186.
- Ji, W. Y., An, M-Z., Yan, G. P., and Wang, J. M. (2007). "Study on reactive powder concrete used in sidewalk system of the Qinghai-Tibet Railway bridge." *International Workshop on Sustainable Development and Concrete Technology*, pp. 333–338.
- Jung, H. K., Jo, H., Park, G., Mascarenas, D. L., and Farrar, C. R. (2014). Relative baseline features for impedance-based structural health monitoring." *Journal of Intelligent Material Systems and Structures*, 1045389X14551435.
- Karmout, M. (2009). "Mechanical Properties of Ultra High Performance Concrete Produced in Gaza Strip." Master Thesis, Islamic University of Gaza.
- Kelham, S., (1996). "The effect of cement composition and fineness on expansion associated with delayed ettringite formation." *Cement and Concrete Composites*, 18(3), 171–179.
- Kusumawardaningsinh, Y., Fehling, E., and Ismail, M. (2015a). "UHPC compressive strength test specimens: Cylinder or cube?" *Procedia Engineering*, 125, 1076–1080.

- Kusumawardaningsih, Y., Fehling, E., Ismail, M., et al. (2015b). “Tensile strength behavior of UHPC and UHPFRC.” *Procedia Engineering*, 125, 1081–1086.
- Lerrard, F. and Sedran, T., (1994). “Optimization of ultra-high performance concrete by the use of a packing model.” *Cement and Concrete Research*, 24(6), 997–1009.
- Luo, H., and Hanagud, S. (1999). “PVDF sensor and its applications in the delamination response detection.” *ASCE Journal of Aerospace Engineering*, 12(1), 23–30.
- Mehta P. K., and Monteiro P. J. M., (2006). *Concrete: Microstructure, Properties, and Materials*. (3rd ed.). McGraw-Hill Companies, NY.
- Mindess, S., Young, F., and Darwin, D. (2003). *Concrete*. (2nd ed.). Prentice Hall, NJ.
- Neville, A. M., (1996). *Properties of Concrete*. (4th ed.). John Wiley & Sons, Inc., NY
- Nguyen D. L., Ryu G. S., Koh K. T., et al. (2014). “Size and geometry dependent tensile behavior of ultra-high-performance fiber-reinforced concrete.” *Composites: Part B*, 58, 279–292.
- Orgass, M., and Klug, Y. (2004). “Fibre reinforced ultra-high strength concretes.” *Proc., International Symposium on Ultra High Performance Concrete*, Kassel University Press, Kassel, Germany, 637–647.
- Park, S., Ahmad, S., Yun, C.-B., and Roh, Y. (2006). “Multiple crack detection of concrete structures using impedance-based structural health monitoring techniques,” *Experimental Mechanics*, 46, 609–618.
- Pyo, S., Wille, K., El-Tawil, S., et al. (2015). “Strain rate dependent properties of ultra-high performance fiber reinforced concrete (UHP-FRC) under tension.” *Cement and Concrete Composites*, 56, 15–24.

- Qiao, P.Z. (2010). “Seismic Performance and Smart Health Monitoring of Concrete with Recycled Aggregate. Part I: Smart Health Monitoring of Concrete with Recycled Aggregate.” Prepared for Transportation Northwest (TransNow), Seattle, WA.
- Qiao, P. Z. (2010). “Seismic Performance and Smart Health Monitoring of Concrete with Recycled Aggregate. Part I: Smart Health Monitoring of Concrete with Recycled Aggregate.” Transportation Northwest (TransNow), Final Report No. TNW2010-05.
- Qiao, P.Z., Zhou, Z.D., and Allena, S. (2017). “Developing Connections for Longitudinal Joints between Deck Bulb Tees – Development of UHPC Mixes with Local Materials.” Final Report to Washington Department of Transportation (WSDOT), Olympia, WA.
- Qiao, P. Z., and Chen, F. L. (2013). “Improved mechanical properties and early-age shrinkage resistance of recycled aggregate concrete with atomic polymer technology.” *ASCE Journal of Materials in Civil Engineering*, 25(7), 836–845.
- Richard, P., and Cheyrezy, M. H. (1994). “Reactive powder concretes with high ductility and 200–800 MPa compressive strength.” *Concrete Technology: Past, Present and Future, Proc., the V. Mohan Malhotra Symposium*, Mehta, P. K. (Ed.), ACI SP 144-24, Victoria Wieczorek, Detroit, 507–518.
- RILEM Technical Committees RILEM TC 162-TDF. (2001). “Test and design methods for steel fibre reinforced concrete – Recommendations: Uni-axial tension test for steel fibre reinforced concrete.” *Materials and Structures*, 34(1), 3–6.
- Ronne, M., and Hammer, T. A., (1999). “Delayed ettringite formation (DEF) in structural lightweight aggregate concrete: Effect of curing temperature, moisture, and silica fume content.” *Journal of Cement, Concrete, and Aggregates*, 21(2), 202–211.

- Roux, N., Andrade, C., and Sanjuan, M. A. (1996). “Experimental study of durability of reactive powder concretes.” *Journal of Materials in Civil Engineering*, 8(1), 1–6.
- Russel, H. G., and Graybeal, B. A. (2013). “Ultra-High Performance Concrete: A State-of-the-Art Report for the Bridge Community”. U. S. Department of Transportation, Federal Highway Administration Publication No. FHWA-HRT-13-060.
- Shaheen, E., and Shrive, N. J. (2006). “Optimization of mechanical properties and durability of reactive powder concrete.” *ACI Materials Journal*, 103(6), 444–451.
- Shetty, M. S. (2005). *Concrete Technology – Theory and Practice*. S. Chand & Company Ltd., New Delhi, India.
- Shin, S. W., Qureshi, A. R., Lee, J. Y., et al. (2008). “Piezoelectric sensor based nondestructive active monitoring of strength gain in concrete.” *Smart Materials and Structures*, 17(5).
- Song, G., Mo, Y.L., Otero, K., et al. (2006). “Health monitoring and rehabilitation of a concrete structure using intelligent materials.” *Smart Materials and Structures*, 15(2), 309–314.
- Song, G. B., Gu, H. C., and Mo, Y. L. (2008). “Smart aggregates: multi-functional sensors for concrete structures – A tutorial and a review.” *Smart Materials and Structures*, 17(3).
- Taylor, H. F. W., Famy, C., and Scrivener, K. L. (2001). “Delayed ettringite formation.” *Cement and Concrete Research*, 31(5), 683–693.
- Tosun, K. (2006). “Effect of SO₃ content and Fineness on the Rate of Delayed Ettringite Formation in Heat Cured Portland Cement Mortars.” *Cement and Concrete Composites*, 28(9), 761–772.
- Tran, N. T., Tran, T. K., and Kim, D. J. (2015). “High rate response of ultra-high performance fiber-reinforced concretes under direct tension.” *Cement and Concrete Research*, 69, 72–87.

- Tseng, K. K., and Wang, L. (2004). "Smart piezoelectric transducers for in situ health monitoring of concrete." *Smart Materials and Structures*, 13(5), 1017–1024.
- USBR. (1992). "Procedure for Direct Tensile Strength, Static Modulus of Elasticity, and Poisson's Ratio of Cylindrical Concrete Specimens in Tension." In USBR 4914. U.S. Department of the Interior, Bureau of Reclamation.
- Wen, Y. M., Chen, Y., Li, P., et al. (2007). "Smart concrete with embedded piezoelectric devices: Implementation and characterization." *Journal of Intelligent Material Systems and Structures*, 18(3), 265–274.
- Wu, F. and Chang, F. K. (2006a). "Debond detection using embedded piezoelectric elements in reinforced concrete structures – Part I: Experiment." *Structure Health Monitoring*, 5(1), 5_15.
- Wu, F. and Chang, F. K. (2006b). "Debond detection using embedded piezoelectric elements for reinforced concrete structures – Part II: Analysis and algorithm." *Structure Health Monitoring*, 5(1), 17_28.
- Talakokula, V., Bhalla, S., and Gupta, A. (2013). "Corrosion assessment of reinforced concrete structures based on equivalent structural parameters using electro-mechanical impedance technique." *Journal of Intelligent Material Systems and Structures*, 25(4), 484–500.
- Yan, S., Sun, W., Song, G. B., et al. (2009). "Health monitoring of reinforced concrete shear walls using smart aggregates." *Smart Materials and Structures*, 18(4).
- Yang, Y. W., Hu, Y. H., and Lu, Y. (2008). "Sensitivity of PZT impedance sensors for damage detection of concrete structures." *Sensors*, 8(1), 327–346.

Zou, Y., Tong, L., and Steven, G. P. (2000). “Vibration-based model-dependent damage (delamination) identification and health monitoring for composites structures – A review.” *Journal of Sound and Vibration*, 230(2), 357–378.